Graduate Theses and Dissertations   Graduate School

2011

Design Issues in Magnetic Field Coupled Array: Clock Structure, Fabrication Defects and Dipolar Coupling

Anita Kumari
University of South Florida, akumari@mail.usf.edu

Design Issues in Magnetic Field Coupled Array: Clock Structure, Fabrication Defects and

Dipolar Coupling

by

Anita Kumari

A dissertation submitted in partial fulfillment
of the requirements for the degree of
Doctor of Philosophy
Department of Electrical Engineering
College of Engineering
University of South Florida

Major Professor: Sanjukta Bhanja, Ph.D.
Sudeep Sarkar, Ph.D.
Syed M. Alam, Ph.D.
Wilfrido A. Moreno, Ph.D.
Paris H. Wiley, Ph.D.

Date of Approval:
January 31, 2011

Keywords: Reliability, Micromagnetism, MCA, Nanomagnet Array, Clock System,
Nanomagnetic Logic

DEDICATION

To my loving Mother

ACKNOWLEDGEMENTS

TABLE OF CONTENTS

LIST OF TABLES

LIST OF FIGURES

ABSTRACT

Even though silicon technology is dominant today, the physics (quantum electron tunneling effect), design (power dissipation, wire delays) and the manufacturing (lithography resolution) limitations of CMOS technology are pushed towards the scaling end. These issues motivated us towards a new paradigm that contributes to a continued advancement in terms of performance, density, and cost. The magnetic field coupled computing (MFC) paradigm, which is one of the regimes where we leverage and utilize the neighbor interaction of the nanomagnets to order the single-domain magnetic cells to perform computational tasks. The most important and attractive features of this technology are: 1) room temperature operation, which has been a limitation in electrostatic field coupled devices, 2) high density and nonetheless 3) low static power dissipation. It will be intriguing to address queries like, what are the challenges posed by the technology with such exotic features? Answer to such questions would become the focus of this doctoral research.

The fundamental problem with magnetic field coupled devices is the directional flow of information from input to output. In this work, we have proposed a novel spatially moving Landauer clock system for MFC nanomagnet array which has an advantage over existing adiabatic clock system. Extensive simulation studies were done to model and validate the clock for different length, size, and shape of nanomagnet array.

Another key challenge is the manufacturing defect, which leads to uncertainty and un-reliability issues. We studied the different dominant types of geometric defects (missing material, missing cell, spacing, bulge, and merging) in array (used as interconnects) based on our fabrication experiments. We also studied effect of these defects on different segments (locations) of the array with spatially moving clock. The study concluded that a spatially moving clock scheme constitutes a robust MFC architecture as location of defect and length of arrays does not play any role in error masking as opposed to conventional clock.

Finally, the work presents the study on the 2D nanomagnet array for boolean logic computation and vision logic computation. The effect of dipole-dipole interaction on magnetization state transition in closely spaced 2D array of ferromagnetic circular nanomagnet was explored. The detailed design space to demarcate the boundary between single domain state and vortex state reveals that the single domain state space is desirable for Boolean logic computation while the space around the boundary would be appropriate for vision logic computing.

CHAPTER 1

INTRODUCTION

1.1 Motivation

The current market trends shows that within the next couple of decades information technology will encompass the way of working, purchasing, playing, seeking service, purchasing products, by providing complete freedom of location to the individual. This will contribute to the necessity of high density storage devices and ultra high run time to access information at high speed. These performance parameters are often characterized by the minimum feature size of the basic component (MOS transistor) of the computer technology. Scaling down the transistor size can then integrate more circuit components in a single chip area with higher operating speed and lower power consumption [1].

The commercially available CMOS has a feature size of 32 *nm* and it is a challenge to scale down beyond 22 *nm*, as predicted by ITRS [1]. This suggests to explore alternative computing method to continue the advancement in the performance. Therefore, there is an urgent need to investigate the nanoscale regime. Our work is one of the efforts in this direction.

Field-coupled Cellular Automata based computing deals with alternative paradigm where, information propagates due to the mutual interaction between neighboring elements as opposed to flow of electrons between two spatial points, generating the promise of very dense, high speed, and low power computing [2]. One of the pioneering efforts in Field-coupled Cellular Automata computing evolved using quantum tunneling interactions of electrons

in neighboring cell [3], promising phenomenal packing density, and the low power-delay product. In a later development, the molecular form of QCA was proposed which works at room temperature [4] alleviating the main drawback of cryogenic operating temperature requirement of E-QCA. The only problem associated with molecular QCA is the difficulty associated with the self-assembly structure. In this dissertation we explored the field coupled computing with nanomagnets for information propagation.

Magnetic phenomena have been extensively explored for information storage and the growth rate of magnetic storage is much faster than the microprocessor, as mentioned by Moore's law. Recently magnetic random access memory (MRAM) development has opened a new direction for high density non-volatile memory, where nanomagnet is used to store bit information and has been successfully integrated with the current semiconductor device. This development encourages the researcher to exploit the nanomagnets for information processing, by utilizing the dipole-dipole interaction between the neighboring element. Hence this magnetic approach promises a novel concept of integrating logic unit and memory in the same chip, in which the same element can store and process data.

The rapid advancement in the high resolution fabrication and measurement techniques makes possible to dig more in the nano world and reveal unknown facts and information. The study of electrical and magnetic properties of nanometer and submicron scale is one of the leading subject in modern magnetism. Today, nanometer magnetic structures using different materials and with controlled dimensions and shapes are fabricated successfully. Although the availability of high resolution MFM and SEM makes characterization of such small dimension structures possible, it is stupendous task to study the dynamics of tiny structures. The nanometer structure behaves differently than the bulk material. Hence deep understanding of nanomgnetic behavior is needed. The micro magnetic modeling plays important role in understanding the dynamics of nanomagnetic structures. Since nanomagnetic computing is a new area, there are limited tool sets available, hence its an

2

important research activity to find and develop the micromagnetic simulation tool to prove the concept of magnetic signal processing.

For past ten years, significant amount of research has been going on magnetic logic concept and produced a promising results. Our group is actively involved in magnetic logic design. We have successfully fabricated nanomagnet system, using E-Beam lithography and characterized the nanomagnets by magnetic force microscope (MFM) [5]. We have also studied the dynamics of nanomagnet with micro-magnetic simulator and successful correlate the theoretical result with experimental data (discussed in chapter 6).

The nano-size structures are more susceptible to defects due to their small size and the fabrication variations. Considering this, reliability study is an essential part in designing tiny magnetic structures. This reseach work would also focus on the defect characterization in the nanomagnet architecture. The research in this work focus on the simulation, modeling and design of nanomagnet network. The open source code, OOMMF by NIST is used and tailored to our purposes.

1.2   Contributions

Our research blends emerging nano scale magnetism with the field coupled paradigm. The contributions to the doctoral research are:

- Design of efficient clock system, independent of the array length: One of the fundamental problem in field coupled computing is the directional flow of information from input to the output. Extra energy in terms of external magnetic field called clock, is required to guide the correct flow of information, irrespective of the type of architecture. Alam et.al [6] first proposed a clock system, called adiabatic clock for magnetic field coupled device. The bottleneck of this clock is the array length, for large array length the clock does not work efficiently for information flow. In order to

overcome this limitation, we have proposed the novel clock system named Landauer clock. This clock utilizes the spatially moving field concept, hence the length of array doesn't affect the signal flow. Furthermore, the clock field strength requirement was studied for different aspect ratio and the scaling factor of nanomagnet

- Defect Characterization of Magnetic field coupled array: Significant research is being conducted on the design methodology of the nanoscale magnetic device to harvest the benefits of small scale structure for computation. The key challenge with such small dimension devices is the manufacturing defect, which leads to the uncertainty and unreliability issues. There is not much study done on defect characterization in magnetic field coupled devices. In this dissertation, we have characterized and modeled the defects observed during our experimental fabrication set-up at the nano-center. We have modeled the defect with both clock systems namely, adiabatic and proposed Landauer clock system. The results showed that magnetic field coupled devices are more robust towards the manufacturing defect.

- The final contribution of this work, is the study of dipole-dipole interaction on the magnetization state transition in finite 2D arrays of ferromagnetic circular nanomagnet. The study investigates the design space for nanomagnet in 2D array that can be used for Boolean logic and vision logic computation. The study concluded that single domain state space is desirable for Boolean logic computation while the space around the boundary would be appropriate for vision logic computing.

This work has demonstrated the applicability of the numerical study for magnetic field coupled nanomagnet architecture, which is a possible strong candidate for next generation, for the computation application.

4

1.3 Organization of this Dissertation

This dissertation is organized as follows,

- Chapter 2 provides the related research works done in the field of field coupled devices for computations.

- Chapter 3 provides the fundamental theoretical background on micromagnetism, which is the the base of this work.

- Chapter 4 explains, in detail, about the clock structure used in the magnetic cellular automata for correct flow of information from input to the output. The spatially varying clock known as *Landauer clock* is proposed in this section. This clock promises correct flow of information irrespective of the array length.

- Chapter 5 explains, in detail, the defect analysis of conventional electron beam lithography fabrication defects and present a simulation based study on their effects on information propagation in a wire.

- Chapter 6 explains, in detail, about the magnetization state transition in closely spaced 2D nanomagnet array for computation application.

- Chapter 7 provides the conclusion and future directions of this work.

CHAPTER 2

RELATED WORK

This chapter deals with a brief overview of current technology limitation, which hinder the continuing advancement in terms of performance and cost in the market. In order to overcome the limitation faced by current technology, some alternative devices and paradigms are described, with special attention being paid to cellular automaton devices, as these relate directly to MCA.

2.1   Current Technology: Limitations

The metal oxide semiconductor - field effect transistor (MOSFET) has emerged over the last 40 years as the predominant technology. It is the basic component used in current digital computer technology. The functional characteristics of a MOSFET are significantly sensitive to dimensional and material factors variations. These include the channel dimensions; gate dimensions; oxide thickness and material; carrier mobility; and doping levels and distribution [7][8].

The industry road-map for CMOS technology development [1] suggests that CMOS technology is facing challenges and predicted fundamental physical limits in near future. Here, some of the key device challenges facing nanoscale CMOS are highlighted that would demonstrate the reason of studying the alternative to current CMOS technology.

2.1.1 Gate Oxide

In MOS technology silicon dioxide (SiO_2) used as the gate dielectric is around 23 nm thick [9]. The oxide thickness will decrease to 1 *nm* in next decade due to the advances in scaling. This in effect will increase in quantum mechanical tunneling [10], which constitutes the leakage current and produce undesirable heating effect. The safe lower limit of oxide thickness is 0.7 *nm* according to muller *et.al.* for acceptable leakage current.

2.1.2 Interconnects

The complexity of wiring increases as more devices are accommodated on a single chip. The RC time delay increases with scaling of wires and this results in signal delay as average distance traveled increases, which affect the RC constant. Since wires can not be scaled aggressively, more layers of interconnects will be required [9]. Fabrication cost will also increase as addition layers of wiring requires an increase in the number of processing step.

2.1.3 Lithography

Conventional CMOS devices are built using a succession of basic lithographic steps [11]. In order to increase the resolution of these processes a decreasing wavelength of light has been used. Current technology uses a 193 nm (ArF) excimer laser to define a minimum feature size of $\sim 0.13 \mu m$. Optical lithography is not likely to extend to the sub-100-nm range [8]. Therefore, future CMOS technology is expected to use techniques such as X-ray, extreme ultraviolet (EUV) or electron beam (e-beam) lithography [12].

2.1.4 Cost

In order to achieve high chip integration and density, the device scaling is reached in nano-scale regime, where fabrication technology has become progressively more complex.
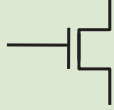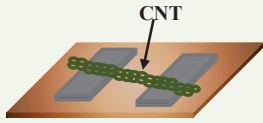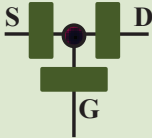
Device		Examples
Current MOS/FET		Si-CMOS
MOSFET: Extension to the End of the Roadmap	CNT	CNT FETs, Nanowire hetro-structure FETs, III-V compound semiconductor and Ge channel replacement
Unconventional, charge-based MOS	S D G	SET (Single electron transistor)
Unconventional, non charge-based beyond MOS devices (ferromagnetic logics)		Moving domain wall devices, Nano magnetic (MQCA) Atomic switch Pseudo-spintronics devices.

Figure 2.1 Review of emerging logic devices.

With the continued miniaturization of device there has been an increase in the cost of building a fabrication facility (or fab). As stated by Moores second law that the cost of a fab increases faster than the growth in the demand for chips [13]. This implies that there must be a point in time when a new CMOS fabrication becomes economically impractical. These costs may curb the continued development of CMOS before technological factors do.

2.2   Emerging Computing Technologies

According to the Moore's law, the fundamental limitations discussed in the previous section have not hit the CMOS scaling limit yet. In order to push the CMOS further, alter-

native implementations have been studied and proposed, for example, vertical replacement gate MOS [14][15][16], high-K gate oxide, 3D MOS, etc. Even-though these development may extend the CMOS life, they would not prevent it reaching the fundamental limits. Hence researcher are motivated to investigate the feasibility of new logic device using innovative ideas, to promise the technology advancement in term of performance and cost. This section assesses briefly, technologies being explored to replace the silicon channel to sustain CMOS performance.

The various emerging devices are listed in Figure.2.1 The alternative devices based on charge transport concepts includes CNTFET [17][18][19][20][21], compound semiconductor nanowire heterostructure [22][23] and SET (single electron transistor)[24][25][26][27][28]. These devices has advantage of high density and low power over CMOS. Since these devices are charge-based logic, the circuits has low error tolerance, limited fan out as compared to the CMOS and the scaling is restricted by the thermodynamic limit. Hence the development of new device based on other than electronic charge is needed, which would extend the scaling of computation logics. The field coupled logic stands against the charge based logic in terms of scaling, performance and density, which includes moving domain wall logic [29][30][31], MQCA, spintronic devices, etc. The remaining part of this section would concentrate more on such type of devices, which is main focus of this doctoral work.

2.3 Field-Coupled Computing: Cellular Automata

In its purest form a CA system is an array of identical interacting units, or cells. The interaction can be electrostatic or magnetic. The state of each individual cell depends on its predefined set of rules and the state of the cells which surround it. Once the initial conditions are set the system is left to evolve towards some sort of equilibrium state.

9

(a)   (b)

(c)
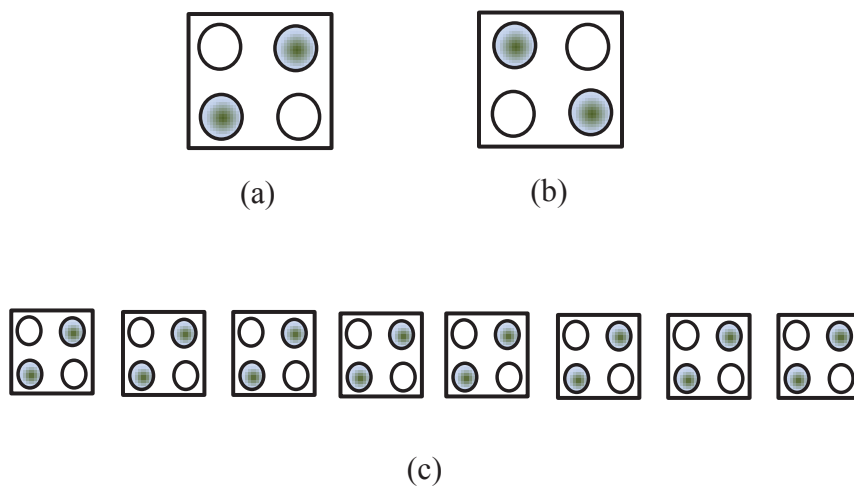
Figure 2.2 The ground state representing (a) logic '0' and (b) logic '1'.

(a)

(b)
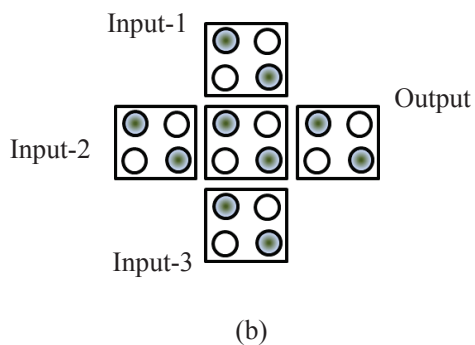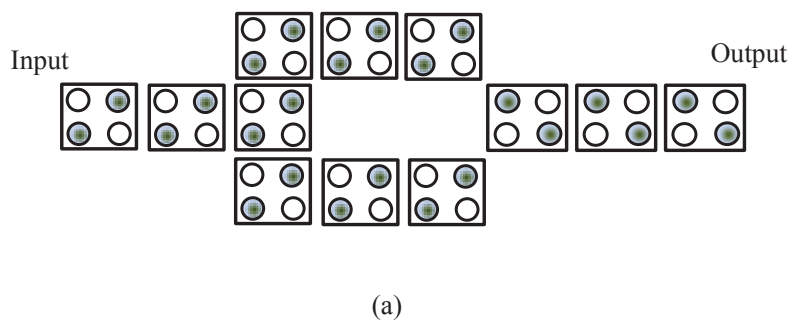
Figure 2.3 The two basic building block of EQCA (a) inverter and (b) majority gate.

2.3.1 Electrostatic-Field Coupled: Electronic Quantum Cellular Automata

The concept of Electronic Quantum cellular Automata (E-QCA) was first introduced by Lent et.al. [3] in 1993. This is an unconventional transistor-less computing paradigm, where an electron tunnel between the nanometer-scale dots, under the influence of electrostatic Coulombic force to realize logic function. The information in E-QCA is encoded in the position of the electron within the dot. A E-QCA cell consist of a coupled-dot with four dots situated at the corners of the square as shown in Figure 2.2. The electron occupy diagonal positions within the cell due to the Coulombic repulsion force. The two possible ground states, represent the stable state of the cell are shown in Figure 2.2 (a). The basic architecture of E-QCA are wire/interconnect as shown in Figure 2.2 (b), inverter and majority gate as shown in Figure 2.3. By arranging the basic cells, all the logic functions can be realized as shown in Figure 2.3. A majority gate in E-QCA is the universal gate, as it can be operated as OR gate and AND gate. The complex circuits like adder, ALU, memories, etc has been demonstrated in [32][33][34][35][36][37]. The advantage of this architecture is low power dissipation, as there is no charge transportation involve during information propagation, causing no current flow. Unfortunately, the need of cryogenic temperature for operation made this technology practically impossible.

2.3.2 Molecular Quantum Cellular Automata

In Molecular Quantum Cellular Automata binary information is represented by charge among redox-active molecular sites. The charge is localized on specific site and tunnel between the sites. The molecular cell coupled to the neighboring cell by coulomb force and hence no current flow required for the information propagation.

The molecule 1,4-diallyl butane radical cation as shown in Figure2.4 is first proposed by Aviram et.al.[38] and stuided by [39][40], consist of two allyl groups in perpendicular
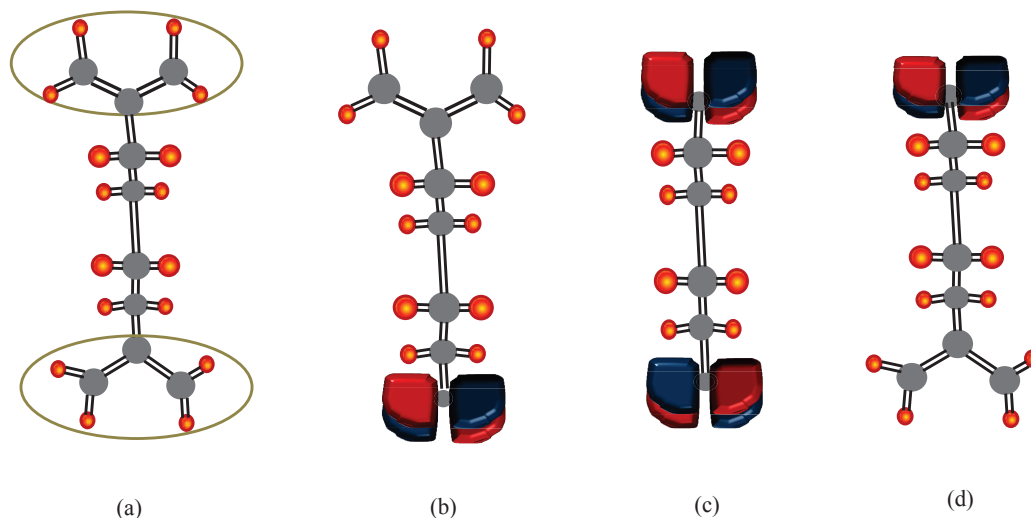
Figure 2.4 Binary logic representation by charge in molecular site. (a) The allyl groups has non bonding levels which act as dots for QCA, (b)HOMO for $+1$ state, where the unpaired electron is in the bottom allyl group, (c) HOMO for the 1-SYM, where the nuclear geometry is symmetric and (d) HOMO for -1 state, where the unpaired electron is in the top allyl group.

to that of the butyl bridge. The molecule radical has two ground sate, with charge localized on either at the top or the bottom allyl group as shown in Figure2.4 (b), (d).

2.3.3 Magnetic-Field Coupled: Magnetic Cellular Automata

In the computer history, ferromagnetic materials have been used to store information in magnetic memories like patterned hard disk drives. Magnetic storage devices were considered to be highly reliable as compared to the semiconductor memories. The biggest breakthrough in magnetic devices was the discovery of GMR (Giant magneto-resistance) by Albert Fert's group in 1988 which led him winning Nobel Prize. Latter this discovery initiated enormous amount of research in spin based electronics known as spintronics. Recently IBM developed the read head sensor based on GMR. Another important development is the magnetic random access memory (MRAM), which can be the good alternative to the hard disk drive. MRAM utilizes the quantum mechanical electron spin phenomenon,

for information storage; wherein the nanoscale magnetic element is embed within the semi-conductor memory. These mentioned development in the magnetic storage devices proved magnetism a strong candidate, hence forced to exploit same for the signal processing. The attractive features of magnetic element based device that fascinated the technologists are:

- Room temperature operation

- Non- volatile nature that is they retain their output state even when the current is switched off.

- low sensitivity to fabrication variations.

- Capability to perform all necessary operation in a same element i.e., storage, logic and amplification.

- Compatible with existing micro-technology.

- Low power dissipation. There is almost zero static power dissipation.

For realistic logic device, in addition to the logic operation, the system has to exhibit several other characteristics. These are:

- ability to propagate information across the corners (at an angle) from the linear direction.

- ability to fan-out the signal, it is a critical element for implementing binary system. It splits the signal in several direction and drive multiple inputs down the line.

- ability to cross over at the intersection of two data wires.

A computational model based on the magnetism is first reported by R.P.Cowburn et.al. [41] [42], wherein networks of interacting circular nanomagnets of radius $\sim$ 100 *nm* are used to
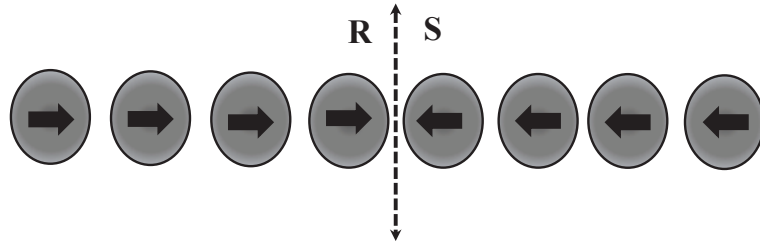
Figure 2.5 A schematic of vector magnetization in nano-dots. A soliton is formed between two opposing direction of magnetization (R and S).
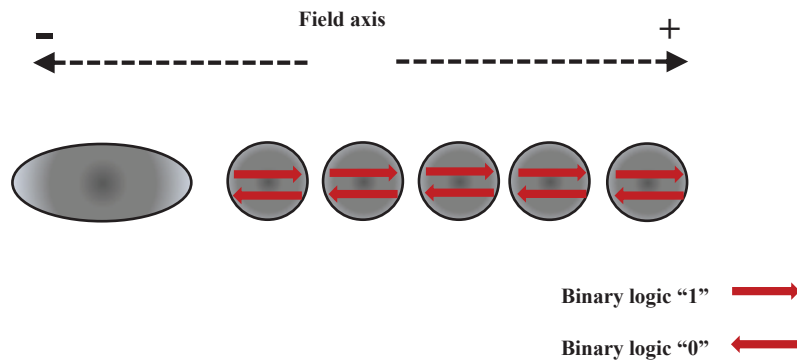
Figure 2.6 Binary state representation in nano-dots. Magnetization along +x-axis represents logic "0" and magnetization along -x-axis represents logic "1".

perform boolean logic operation and propagate information, by means of a *magnetic soliton*. A soliton is a high energy region (as shown in Figure 2.5), which occurs when two neighboring elements have anti-parallel magnetization, and moves along the array through sequential magnetization reversal.

The soliton motion can be controlled by the applied magnetic field. In Cowburn *et.al.*, the nano-dots has zero shape and magneto-crystalline anisotropy, and magnetos-static interaction between the dots ensure that the moments of the dots points either parallel or anti-parallel with the axis of the array, which is used to represent boolean logic state as shown

14

	Applied Field	
	0	1
Input nano-dot 0	0	0
1	0	1

Figure 2.7 Truth-Table of nano-dots of Cowburn's logic device.

in Figure 2.6. In this architecture magnetization orientation of nano-dots are strongly influenced by the left most dot, having easy-axis anisotropy along the direction of the array. An oscillating magnetic field is applied, which is biased in the x-axis.

If the direction of the bias field is considered as one input, along with the input dot then the system of dots act as an AND gate as shown in Figure 2.7. it is depicted from the truth table that when the input dot is at "1" logic, the nano-dots switches in accordance with the oscillations of applied bias field between "0" and "1" logics. While input dot with logic "0" does not change the nano-dots, with oscillation of applied field.

The Cowburn's model discussed above is efficient for simple logic operations. However the model is not suitable, if logic operation required to bend around the corners or to fan-out in different directions, this is due to lack of shape anisotropy in the nano-dots. The improvement over this model is achieve by utilizing the shape anisotropy of the array elements [**?**], wherein the soliton motion behavior is investigated in an array of square element of permalloy. The square element posses easy axis at 45 degree and external field is applied at an angle of 30 degree. This helps the soliton motion to propagate linearly as
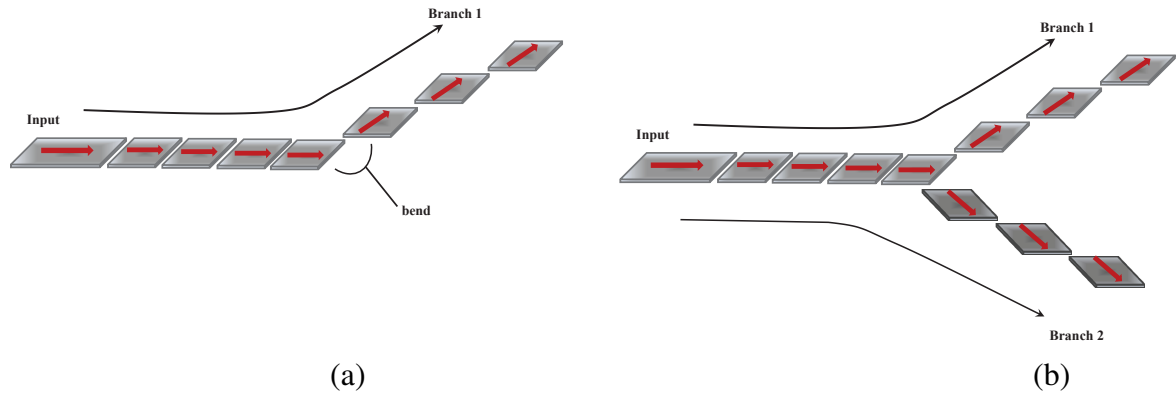
Figure 2.8 Schematic representation of signal splitting in square nanomagnet. (a) soliton propagation in bent chain of square nanomagnet, with branch at 45 degree to x-direction and (b) soliton representation in Y-shaped chain, information is bifurcated in two branches namely branch 1 and branch 2.

well as around the bend as shown in Figure 2.8 (a). Further, the fan-out, splitting of signal is investigated, where soliton flows at Y shape fork as shown in Figure 2.8 (b). The path of soliton is controlled by the sequence of external applied field and its direction.

Another successful model, which utilizes the uniaxial shape anisotropy property of nanomagnet is studied by Csaba and also have done in this dissertation. Csaba *et.al.* [43][44][45] proposed the logic states signaled by the magnetization direction of the single-domain magnetic pillar dots. The dots couple to their nearest neighbors through magneto-static interactions, try to align anti-parallel ground state or minimum energy state Figure 2.9(a) or higher-energy metastable state Figure 2.9(b), which is not desired for correct operation.

MCA offers very low power dissipation [46] and high integration density of functional devices. In addition, it can operate over a wide temperature range from near absolute zero to the Curie temperature of the employed ferromagnetic material. A nanomagnet logic device consists of a finite number of dots. Figure 2.10 illustrates two basic building blocks that would be used to construct MCA circuits. A wire or interconnect is a line of nanomag-

16

Figure 2.9 (a) Definition of logic '1' and '0' for nanomagnets and (b) Metastable states for coupled pairs.
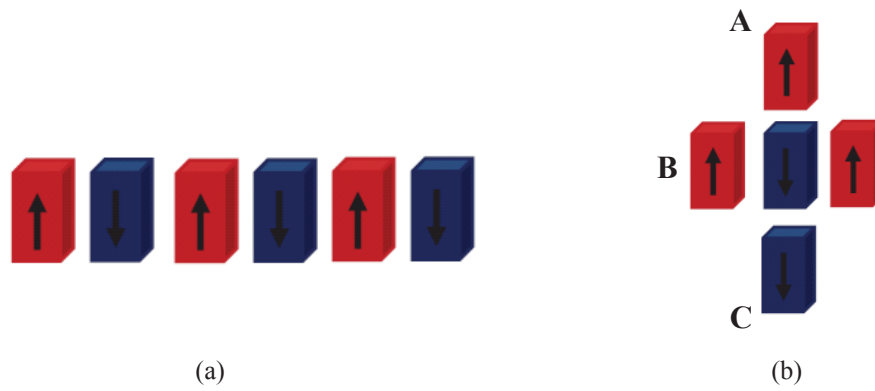
Figure 2.10 (a) Inverter (b) Majority gate.

A	B	C	Z	
0	0	0	1	N O R
0	0	1	0	
0	1	0	0	
0	1	1	0	
1	0	0	1	N A N D
1	0	1	1	
1	1	0	1	
1	1	1	0	

Figure 2.11 Truth-Table of NAND and NOR gates using majority gate. If A=0, the magnetic gate performs logical NOR operation and if A=1, it performs NAND operation.

net that is anti-ferromagnetically coupled with the neighbor element. This array of MCA can be used as inverter as shown in Figure 2.10(a), the number of nanomagnet in an array decides, its operation as wire or as an inverter. The basic logic gate in MCA is majority gate as shown in Figure 2.10(b). The output of majority gate is dependent on the majority of the 3-input. The same majority gate can be used to perform NAND or NOR operation citeendo, by setting one input of the gate to logic '0' or '1' as shown in Figure 2.11. These basic building blocks have been experimentally demonstrated [47] [48] [49]. The MCA architecture has the ability to fan-out the signal, first demonstrated by Varga *et.al.* [50]. In fan-out circuit the input nanomagnet dictate the state of the output nanomagnet as shown in Figure 2.12. Another interesting realization of MCA system is coplanar cross wires, experimentally demonstrated by Pulecio *et.al.* [5], where two data wires cross over at intersection without signal loss as shown in Figure 2.12 (b).

The clock for MCA using adiabatic scheme [6], power analysis [51] has already been studied, predicting MCA a promising architecture. Defect study by Niemier *et. al.* mostly
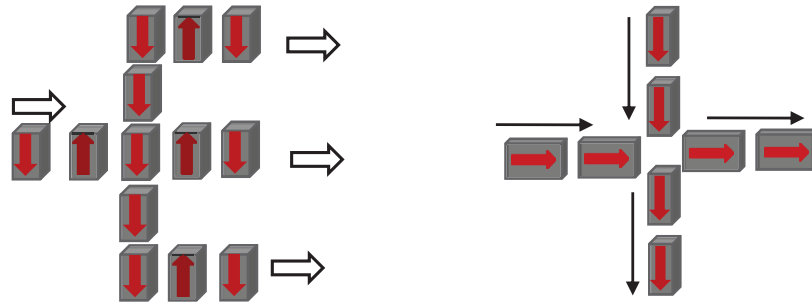
Figure 2.12 (a) Schematic of the fan-out circuit implemented for nanomagnet and (b) Representation of cross wire.

focuses on individual defective magnets using adiabatic clock. For bulge defects, all the magnets in an array were assumed to be wider. In Kumari *et. al.* [52], the effect on single defects on the entire array was studied. We also found in [52] that the defect was masked unpredictably which led to look at the new spatially moving clock [53], which is discussed in detail in chapter 4. In this work, we also report the extensive defects (missing material, missing cell, bulge, merge cell, irregular space) that are observed in-house in our nano-center during the fabrication of the MCA arrays and study the masking effect in the presence of a spatially moving clocking field.

CHAPTER 3

THEORETICAL BACKGROUND

This chapter concentrates on the basic physical phenomena corresponding to the magnetic aspect of this work. The chapter will be discussing the magnetic theory, equations and magnetic behavior of the materials. The factors that are significant in nanoscale magnetic structure is explained in this section. The magnetic interactions and various energies within small elements, which demonstrate the different aspect of magnetic elements, like shape anisotropy and how as characteristic size reduces, multi-domain particles switches to single domain structure.

3.1 Micromagnetics

Micromagnetics is a phrase, first introduced by Brown over 50 years ago, put together the concepts previously developed by Weiss, Landau and Lifshitz. A complete understanding of ferro- and ferrimagnetic structures of length scale of sub-micron meter can be obtained using the micro-magnetic theory. Regarding the presented work in this dissertation, it provides the fundamental theoretical understanding to the design of magnetic logic architectures.

3.1.1 Exchange Energy

The exchange interaction is purely quantum mechanical and has no classical analogue, which arises from the short range interaction called *exchange coupling*. Heisenberg pro-
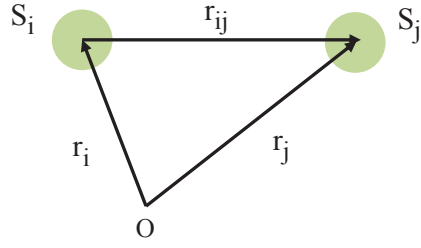
Figure 3.1 Representation of the interaction between two adjacent spins Si and Sj.

posed a quantum exchange interaction in 1928 to account for the residual magnetism of ferromagnetic samples in zero applied field [54]. If S_i is the total electron spin at lattice site i and S_j at site j, then Heisenberg suggested that the exchange energy is proportional to the dot product of these values as shown in Figure.3.1.

The actual origin of the interaction mechanism relies on a coupling between the conduction s-electrons and the d-electrons in the ferromagnetic material. The latter electrons are responsible for the magnetism itself. As can be seen in Figure.3.2 (a), the s-band typically possesses a symmetrical density of states (DOS) distribution, with respect to spin-up and spin-down electrons. In contrast, the d-electrons have asymmetrical DOS,where one sub-band is shifted with respect to the other by the amount of the exchange energy, E_{ex}.

For the purpose of this dissertation, it is sufficient to know that the interactions between spins can be described classically by the following dot product:

$$E_{ex} = -2 \sum_{i,j=1}^{nn} J_{ij} S_i . S_j \tag{3.1}$$

where *nn* stands for the nearest neighbors. The exchange integral J_{ij}, depends on the distance between the interacting spins, its sign determining a parallel (ferromagnetic) or
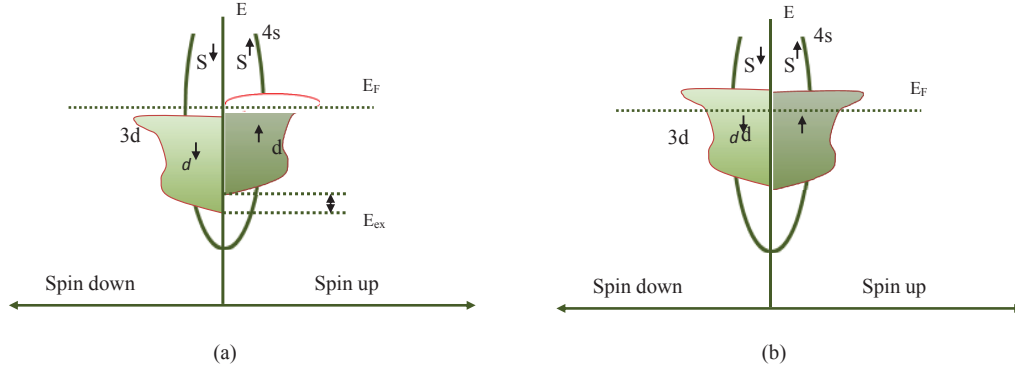
Figure 3.2 A schematic representation of the density of states D(E) of the 4s and 3d bands of a ferromagnetic material at (a) T < TC and (b) T > TC. In (a) the material is ferromagnetic. Spin-splitting of the d band due to the exchange interaction results in an imbalance of electron spin populations at the Fermi level. In (b) the material is paramagnetic with equal electron spin populations at the Fermi energy level EF.

anti-parallel (anti-ferromagnetic) ordering. J_{ij} is related to the overlap of the magnetic orbitals of adjacent atoms and to the Pauli exclusion principle.

$$E_{ex} = \int A_{ex}[(\nabla m_x)^2 + (\nabla m_y)^2 + (\nabla m_z)^2]d\tau \qquad (3.2)$$

where A is known as the exchange stiffness (or exchange constant):

$$A_{ex} = \frac{nJS^2}{a} \qquad (3.3)$$

Here a is the lattice constant and n is the number of atoms in a unit cell. For example $n = 1$ for a simple cubic lattice and $n = 2$ for a body-centered cubic lattice [55].

The parameter A_{ex} (J/m) is called the exchange constant. In the simple case of a cubic crystal, A_{ex} is JS^2/a, with a the crystalline lattice constant. Through its dependence on the lattice constant, the exchange constant is also temperature dependent. A perfect

alignment of the magnetic moments corresponds to a minimum of the exchange energy ($E_{ex} = 0 J/m3$).

3.1.2 Zeeman Energy

The Zeeman energy is the potential energy of the atomic moments of a ferromagnetic sample when an external magnetic field is applied. When an external field is applied, the magnetization will tend to align with the field in order to minimize the potential energy. If the magnetization deviates from this equilibrium orientation an increase in the potential energy results. The energy penalty is proportional to the angle between the magnetization and the field, thus the Zeeman energy per unit volume is

$$E_z = -MH_Z \tag{3.4}$$

The external field in Equation 3.4 may not necessarily be a steady bias field between the poles of an electromagnet, for example, the field may be a time varying pulsed or harmonic field.

3.1.3 Magneto-static Energy / Dipole-dipole Interaction

The magneto-static interaction is related to Zeeman energy, the interaction of the material with itself is magneto-static energy whereas the interaction with the external magnetic field is the Zeeman energy. The magneto-static energy arises from the stray magnetic field and concerned with the long range magneto-static interaction of atomic moments with the magneto-static fields of the other atomic moments within a ferromagnetic sample. The magneto-static energy can be expressed as:

$$E_{demag} = -\frac{1}{2}H_d.M \tag{3.5}$$
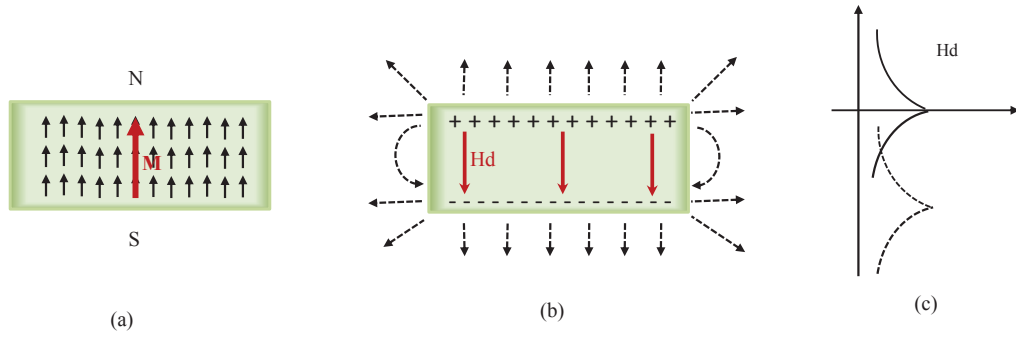
Figure 3.3 Magnetic pole distribution in finite size magnetic element. (a) Magnetic dipoles inside a magnetised sample, (b) Free mag- netic monopoles at surfaces and (c) Variation of the amplitude of the perpendicular component of the internal field with position inside the sample, in the case of a thick sample.

3.1.3.1 Demagnetizing Field (H_d)

When a magnetic sample of finite size is magnetised, free magnetic poles are induced on the both its end as shown in Figure.3.3. These, in turn, give rise to magnetic field in a direction opposite that of magnetization as shown in Figure.3.3 (b). This field, H_d, going from north pole to south pole inside the sample. This field is express as:

$$H_d = -\nabla U \tag{3.6}$$

Where U is the magneto-static potential, given by,

$$U(r) = -\int \frac{\nabla'.M(r')}{|r-r'|}dV' + \int \frac{n.M(r')}{|r-r'|}dS' \tag{3.7}$$

Where ∇' contains derivative with respect to the component of r'. Similarly with electrostatics, the sources of the demagnetizing field are the volume or the surface magnetic charges associated to the magnetization distribution inside a magnet. The magnetic charges are analogous to the electric ones, with the difference that they always appear in pairs, a

magnetic charge being always balanced by one having the opposite sign. The first term in Equation.3.7 can be interpreted as a contribution due to a volume charge density $(-\nabla.M)$, while the second term is a contribution due to a surface charge density $(n.M)$, where n is a surface normal vector. In significantly large external magnetic field, the magnetization is uniform and the volume term in Equation.3.7 vanishes, as $\nabla.M = 0$. The demagnetizing field is then

$$H_d = -\nabla U = -M\nabla + \int \frac{n}{|r-r'|} dS' \tag{3.8}$$

Which is linear in the magnetization of M. Furthermore, from Equation.3.5 and 3.8, the demagnetizing field can be written as:

$$H_d = -N(r) \cdot M \tag{3.9}$$

Where $N(r)$ is the demagnetizing tensor.

3.1.4 Anisotropy Energy

Magnetic anisotropy describes the dependence of the internal energy on the direction of spontaneous magnetization. Therefore, there is a preferred direction for the magnetization to align, which is known as easy axis and lower in energy than hard axis. There are several sources of the anisotropy: magneto-crystalline, surface and interface anisotropy, strain anisotropy, shape anisotropy and growth induced anisotropy.

3.1.4.1 Magneto-crystalline Anisotropy

The most common source of anisotropy is due to the inherent crystal structure of the material and is therefore called magnetocrystalline anisotropy. Due to spin-orbit interactions the electron spins prefer to align parallel to a specific crystalline axis. Uniaxial

behaviour means that there is a single easy axis and the anisotropy energy is a minimum when θ (the angle between the easy axis and the direction of the magnetization) is zero or π. It is usually sufficient to consider only the first few terms of the anisotropy energy density model (often only the first term is required):

$$E_{anisotropy} = \int K_1 Sin^2\theta + K_2 Sin^4\theta + ...d\tau \qquad (3.10)$$

The magneto-crystalline energy is smaller as compared to the exchange energy. Also magneto-crystalline interaction is short range that results in a random distribution of local easy axis.These can average out and often result in little or no magneto-crystalline anisotropy when the whole system is considered. However, this is complicated in submicron elements where the small number of grains involved can lead to the random distributions not canceling each other out. Moreover, it is a consequence of the material's crystal structure, so anything which affects the crystal structure (strain, impurities or dislocation) will influence the magneto-crystalline anisotropy and is independent of the sample geometry.

3.1.4.2 Shape Anisotropy

In submicron sized magnetic sample, the geometry of an element causes another type of anisotropy, which reduces the magneto-static energy by aligning the magnetization along a particular axis, is called shape anisotropy. Consider a uniformly magnetized sample. Inside the element the parallel configuration of the dipoles means that their north and south poles effectively cancel each other out. This minimizes the number of volume poles. However, this configuration does produce a surface magnetization due to what can be thought of as uncompensated, free surface poles. These give rise to a demagnetizing field which points in the opposite direction to the internal magnetization. As illustrated in Figure.3.4, different
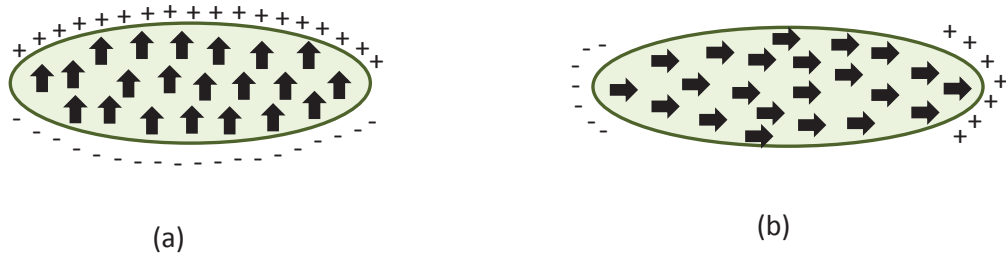
Figure 3.4 Uniformly magnetized ellipsoid exhibiting two magnetization orientations. (a) magnetization lies parallel to the short axis (y axis) there is large number of uncompensated free poles, which results in a large magneto-static energy. This axis is therefore called the hard axis. (b) magnetization lies parallel to the long axis (x axis), then there is a low number of uncompensated free poles. Therefore this has a low magneto-static energy and is know as the easy axis.

orientations of the magnetization give rise to different numbers of free poles. The more surface poles which are created the greater the demagnetizing field. The magneto-static energy term attempts to reduce the number of uncompensated free poles in the sample. In general, the longest dimension of a particle forms the easy axis. Therefore, the situation illustrated in Figure. 3.4 (a) (magnetized along the y axis) has the greater energy of the two configurations shown.

3.2 Static Micromagnetics: Equilibrium / Ground State

The various energies that were explained in previous section are assembled, which contributes to the total free energy of the magnetic sample, can be given as:

$$E_{total} = \frac{1}{2} \int_v H_{eff} M dV \qquad (3.11)$$

In micromagnetism, the aim is to find a distribution of magnetic moments that minimizes the total free energy function (Equation.3.11). The equilibrium magnetization distribution

satisfies two conditions:

$$\delta E(m) = 0; \tag{3.12}$$

$$\delta^2 E(m) > 0$$

The second equilibrium condition *-the torque condition-* deduced by Brown [56], states that at equilibrium, the torque from the effective field acting on the magnetic moment m must be nil everywhere.

$$m \times H_{eff} = 0 \tag{3.13}$$

3.3 Dynamics of Magnetization: Landau-Lifshitz Equation

The equations deduced by Brown (Equation3.13) is significant to define the equilibrium state of the magnetic element,but it does not answer how the system reaches this state. The magnetization dynamics, which explains the magnetization distribution $M(r,t)$ change in time under the influence of effective magnetic field H_{eff}, can be explained through the L̂andau - Lifshitz - Gilbert equation. In order to deduce this equation, the start point is:

$$\frac{d\mathbf{M}}{dt} = -\gamma \mathbf{M} \times \mu_0 \mathbf{H_{eff}} \tag{3.14}$$

describes the magnetization's gyro-tropic reaction in the presence of the field H_{eff}. Where γ is the gyro-magnetic ratio of the free electron ($\gamma = 2.210 \times 10^5 T^{-1} s^{-1}$). From Equation.3.14, the torque induces a rotation of M, with angular velocity $w = \gamma \mu_0 H_{eff}$. In this processional motion as shown in Figure.3.5 (a), the modulus of the magnetization remain unchanged during motion and the angle between the field and the magnetization also remain constant as a function of time.
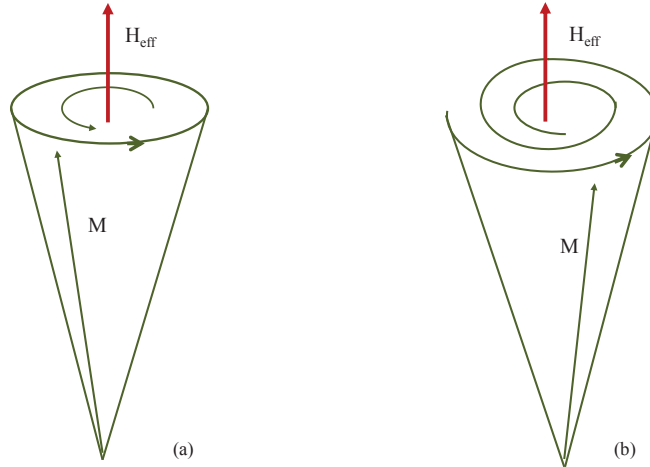
Figure 3.5 Precession of the magnetization vector M around the effective magnetic field H_{eff} (a) without damping ($\alpha = 0$) and (b) with damping ($\alpha > 0$).

The spin of the electron on the atom cause precession of spins on the neighboring atom, which change the spin on their neighbors. This is called spin diffusion, mechanism of loss of energy from the atom in whatever field it is precessing. The Equation.3.14 does not describe the dissipation process resulting in a parallel alignment of M and H_{eff}. In order to include the relaxation of M towards the ground state, Gilbert introduced a damping term, that replaces the field H by an effective field, including an ohmic type dissipation term,

$$H_{eff} = H - \alpha \frac{1}{\gamma_0 M_s} \frac{d\mathbf{M}}{dt} \tag{3.15}$$

The resulting dynamic equation of magnetization motion is:

$$\frac{d\mathbf{M}}{dt} = -\gamma[\mathbf{M} \times \mathbf{H_{eff}}] - \frac{\alpha\gamma}{M_s}[M \times (M \times H_{eff})] \tag{3.16}$$

This equation is known as Landau - Lifshitz , where M_s is the saturation magnetization and α is a phenomenological damping parameter. The basic LL equation assumes that the effect of damping is minimal and the precessional term dominates. However the damping

(a)

(b)

(c)

(d)
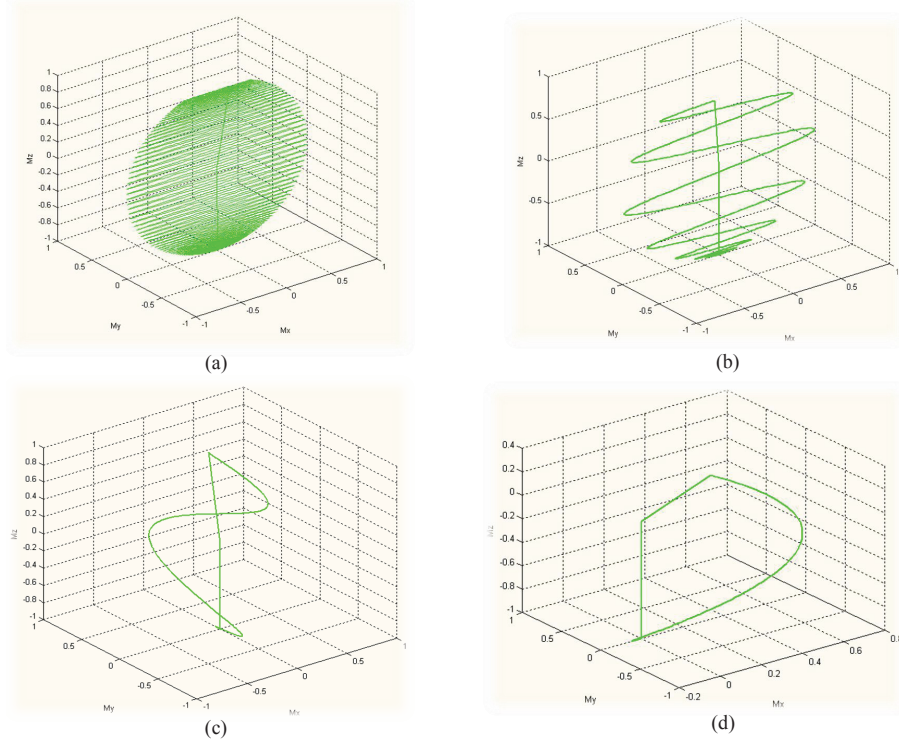
Figure 3.6 Trajectory of the magnetization vector of a single-domain particle for different α values . The precession was initiated by a strong external field pulse along positive x-axis.

term controls the precession process and can not be ignored. The damped movement is shown in Figure.3.5 (b), where magnetization spiral down until it aligned with the field, resulting in zero torque on M. The precession of the magnetization will go endlessly, without the damping as shown in Figure.3.5 (a). Therefore Gilbert presented the more general theory, which considers the damping of the precessional motion. Equation3.17 is known as Landau - Lifshitz -Gilbert (LLG) equation:

$$\frac{d\mathbf{M}}{dt} = \frac{-\gamma}{(1+\alpha)}[\mathbf{M} \times \mathbf{H_{eff}}] - \frac{\alpha\gamma}{M_s(1+\alpha)}[M \times (M \times H_{eff})] \tag{3.17}$$

If α is small, then it will precess through several circle before reaching the equilibrium state as shown in Figure.3.6 (a). On the other hand if α is large, the magnetization vector immediately falls into the effective field vector, as shown in Figure.3.6 (d). For most materials, the damping parameter α is around: $0.01 - 1.0$.

3.4 Superparamagnetism

At temperature T each spin is subjected to thermal agitation, the energy of which is $KT/2$ (2×10^{-14} ergs) per degree of freedom of motion. As the temperature increases in a system, thermal perturbations increasingly disrupt the inter spin interactions. The Zeeman energy associated with a spin of one Bohr magneton (a basic magnetic unit with $m_B = 9.3 \times 10^{-21}$ $ergs.G^{-1}$) in an external field of a few hundred Oersted, is approximately 10^{-17} ergs. Considering these two values it is immediately apparent that thermal perturbations are much larger than Zeeman (and magneto-static) terms and that if exchange did not dominate over short range no ferromagnet would display net magnetization at room temperature. However, if, the volume of the particle is very small that the height of the potential barrier K_u at H= 0 is of same order of magnitude as $KT/2$, then magnetization is expected to be activated to overcome the potential barrier. This state is named as superparamagnetism. For the critical volume v_0, $v_0 K_u \sim KT/2$, calculated value of v_0 at temperature $T = 273K$ and $K_u = 10^5$ J/m^3 is:

$$v_0 = \frac{KT}{2K_u} = \frac{3.77 \times 10^{-21}}{2 \times 10^5} = 1.9 \times 10^{-26}$$

At superparamagnetism, exchange interactions are preserved but the thermal excitations causes rapid and continuous switching of the direction of the magnetization in a particle.

31
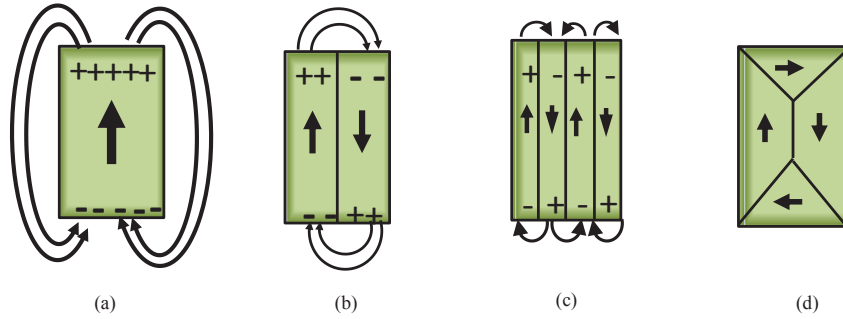
Figure 3.7 Magnetic domain structures in a rectangular ferromagnet. The magneto-static energy is significantly reduced for the last case where a closure domain configuration is clearly visible.

Time dependent switching is described by the Arrhenius-Neel law:

$$\tau = \tau_0 \ exp\frac{K_u v}{KT} \tag{3.18}$$

Where,τ is average time in which switching occurs, τ_0 is the inverse of the attempt (or the Neel attempt) frequency. The value of τ_0 is usually estimated as $\approx 10^{-9}$ s (the reciprocal of the gyro-magnetic resonance frequency). If $K_u v \approx KT$ then the value of τ becomes very small. The moment repeatedly flips between the two stable states, spending only a short period of time in each minimum before switching again. It therefore retains $|M| \approx \Sigma_i^N m_i$, but the time average measurement of M is zero.

3.5 Domain Wall Theory

Domain wall attributes to a transition region which separates adjacent domain magnetized in different direction. The change in magnetization from one domain to a neighboring domain does not occur in one discontinuous step but it takes place gradually through the boundary.The total angular displacement across a wall is commonly 180 degrees or 90 degrees, that can occur at relatively low external magnetic field. The reason for the formation
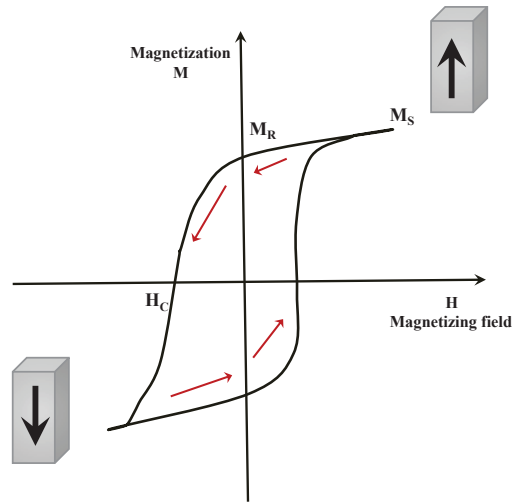
Figure 3.8 Magnetic hysteresis curve M vs. H.

of the domain structure is that the potential energies (exchange energy and magneto-static energy) associated with the magnetized sample is thereby minimized. It is in spite of the cost in energy of forming the domain walls. The competition between the opposing influences of exchange energy and magneto-static energy determine the thickness of a domain wall. Figure 3.7 shows how domain formation can minimize the magneto-static energy. A single domain magnetic structure has high magneto-static energy due to accumulation of magnetic charges at the extremities of the domain as shown in Figure 3.7 (a). Splitting this domain in two or more domain of equal area each, with magnetization oriented up and down, the overall magnetization is zero as shown in Figure 3.7 (b), (c).

3.6   Magnetic Hysteresis Loop

Magnetism exhibits a large variety of configurations, depending on the different energy intensities. The evolution of these configurations, while applying a external field, is of great interest. Many of the parameters describing this evolution can be determined by looking at the induction field (M) dependence on the external field (H). This function (M(H)) is

33

called the magnetization curve, or hysteresis loop. Figure 3.8 shows a typical example of such a loop. Important parameters can be extracted from this curve :

- Saturation magnetization (M_S) - the maximum possible magnetization value of a material that can be achieved with a magnetic force.

- Remanent magnetization (M_R) -It is the magnetization value that remain in material when the magnetic field is removed. The remanent magnetization is known as retentivity when the material has been magnetized to saturation point.

- Coercive field (H_C) - It is the amount of reverse magnetic field that must be applied to a magnetic material to make the magnetic flux return to zero.

3.7 Numerical Micromagnetism

The above discussed energy terms and micro-magnetic equations (LLG), which describes the dynamics of magnetization are nonlinear in nature and difficult to solve. The traditional analytical method gives an accurate estimation of characteristic behavior of simple uniform magnetic structures, under simplest ambient conditions. In order to investigate and understand the physical phenomena of complex non-uniform magnetic structure, numerical simulation study must be useful.

The numerical method is based on the splitting up the magnetic element into small discrete cells, the micro-magnetic (LLG) equation is solved for each discretization elements. The choice of discretization cell is very important, as it affect the accuracy of the result. The choice of cell size is based on the two characteristic lengths namely, 1) the exchange length (l_{ex}), which determine the competition between the exchange and magneto-static energy and 2) the bloch length (l_B), this quantifying the competition between exchange and magneto-crystalline interaction.

$$l_{ex} = \sqrt{\frac{2A_{ex}}{\mu_0 M_S^2}} \qquad (3.19)$$

$$l_B = \sqrt{\frac{A_{ex}}{K}} \qquad (3.20)$$

In numerical simulations the dimension of the discretization element must be smaller than the above two characteristic lengths. The smaller cell size results in more discretization element for the given sample, which increase the simulation run time.

3.8 Object Orientated Micro-magnetic Framework - OOMMF

In this dissertation, all the numerical simulations were carried out using the Object Oriented Micro-magnetic Framework (OOMMF) code developed by M.Donahue and D.Porter at National Institute of Standards and technology (NIST). OOMMF is portable, extensible and freely available to public. OOMMF uses the finite difference (FD) approximation method to solve the LLG equation, where the system is space-discretized by the repetition of regular-shaped mesh cell. The recently updated version of OOMMF has ability to simulate 2D and 3D system with 2D and 3D space discretization as shown in Figure 3.9. In 2-dimensional system, the space discretization contain N_x cell along x-axis and N_y cells along y-axis. For the 3D structures, the mesh contain N_x x N_y x N_z cells.

Simulations in OOMMF runs according to a hierarchy as mentioned below:

1: Input element geometry dimensions and mesh cell size

2: Input material parameters: A, M_s, K
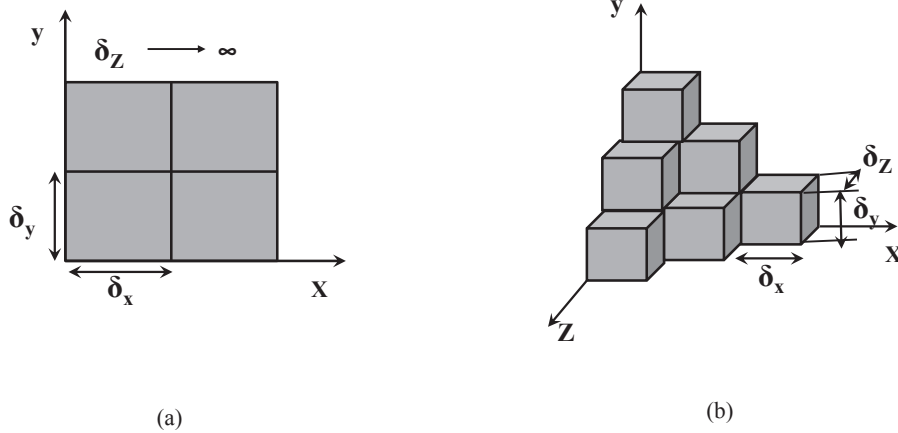
Figure 3.9 Finite difference discretization (a) 2D and (b) 3D.

3: Stopping criteria m x h x m, dm/dt

4: Calculate evolution of magnetization with LLG equation

5: **if** Stopping criteria = = FALSE **then**

6:    Go to step 4

7:    **if** Last Stage = =FALSE **then**

8:       Introduce appropirate parameter, if any

9:       Go to step 4

10:    **end if**

11:    Stop

The package perform simulations in large increments called stage, wherein each stage is run in small increments called iterations. The iterations are controlled by the evolver, which is responsible for the magnetization configuration of the element from one step to another. The evolver is further controlled by the drivers. The driver handles the stages and track the simulation evolves as a whole. The conditions for example applied magnetic field, are introduced at the beginning of the stages. The evolver updates the magnetization configuration of the element after each stage. The length of each stage

is user-defined that constitutes the stopping criteria in the driver. A new stage begins, once the stopping criteria meets.

OOMMF package has two types of driver-evolver pairs. Each evolver must be matched with the appropriate driver type. The first type is minimization evolver-driver, which locate local energy minima of the system through direct minimization technique. Second pair is the time evolver-driver, which keep track of the time evolution of the magnetization according to the Landau-Lifshitz-Gilbert (LLG) equation.

The OOMMF code has been extensively used by the research community which generate and use the simulated data for better understanding of the magnetization dynamics at nanoscale. The previous studies and several research papers has compared OOMMF simulation results to the experimental data [57][58][59] and assured that the details of the code is correct. Since it is an open source code, one can easily tailor the code to the specific requirements.

CHAPTER 4

CLOCKING SCHEME FOR MCA ARRAYS

The chapter will be discussing the need of extra energy called clock, in field cou-
pled architecture for correct propagation of information from input to output without
magnetic frustration. In addition to the existing clock system, in this work the spatially
moving Landauer clocking scheme for MCA arrays (length of eight, sixteen and thirty-
two cells) is explored. Simulation performed in OOMMF suggests that the clocking
field is sensitive to scaling, shape and aspect ratio.

4.1 Clock System

Regardless of the implementation, a circuit or system made from QCA devices will
realistically require some kind of clock structure that directs the computation and pro-
vides gain. A nanomagnet of pillar shape has two possible stable state along its easy
axis, which corresponds to energy minima or ground state. For complicated network
of nanomagnets, the global ground state attained when all the nanomagnet are aligned
in anti-parallel to their neighbors, attributes to correct flow of information. However
there is a possibility of metastable state, which represent local minima on energy curve
as shown in Figure 4.1. The metastable state causes incorrect ordering, which results
in the incorrect output. Hence ground state configuration at room temperature does not
prove to be stable.
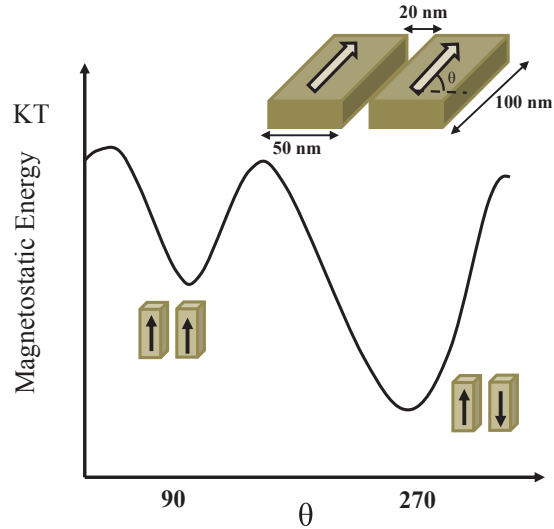
Figure 4.1 The graph shows the total magneto-static energy of a system of two coupled single-domain permalloy nanomagnetic pillars, as a function of the magnetization of the right dot. The magnetization of the left magnet was kept fixed.

In order to achieve correct ordering of nanomagnet to attain well defined final state, varying external clock field is required. Moreover, magnetic interactions are direction-insensitive, we need an addition control apart from input to drive the information flow from input to output. The clock helps the system to overcome the energy barriers between metastable states and the ground state.

4.2 Adiabatic Clock

In Magnetic QCA, first clocking scheme is proposed by Alam et.al, where periodically oscillating external magnetic field is applied along the hard axis (X-axis) of group of nanomagnets [51] as illustrated in Fig. 4.2. In Fig. 4.2 the first (or top) line(or wire) of nanomagnets illustrate the ground (or minimum energy) state. The middle line (or wire) is unstable state, all the magnetic moments are align in the direction of external magnetic field (clock). when the external magnetic field is removed, the nanomagnets
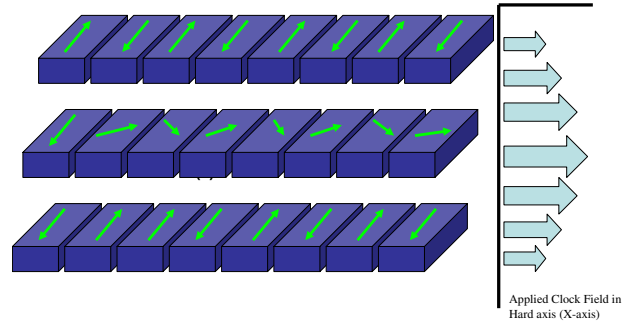
Figure 4.2 Adiabatic Operating scheme of a wire: (a) initial configuration, (b) high-field (null) state, (c) after the application of the input, and the final ordered state.

tries to align into anti-ferromagnetically ground state as shown by Fig. 4.2, bottom line (or wire).

From our simulation experiments, we observed that even though the previous scheme is easy to implement and works well for short array (upto length 4), larger array of nano-magnets cannot be clocked through the above scheme. Fig. 4.3 (B) demonstrates the frustrations in 8 MCA array of size 60 x 90 x 20 nm^3 (width x height x thickness), using this clock scheme where the entire set was driven to hard axis at the same time and released adiabatically (all of them at the same time). We gave 70mT field along hard axis and then reduced the field adiabatically and finally to 0mT. One can easily observe that magnets (2 & 3) and magnet (7 & 8) are reaching a meta-stable state which are not anti-parallel.

The second experiment revolved around dividing the magnetic array and using the multistage clocking as suggested by Alam *et. al* in [6] [51] where each clock state has group of nanomagnet. The magnetic field is applied (in hard x-axis) and released from the hard axis simultaneously. We tried with two clock state, each consisting of 4. During first clock state the first 4 magnet experience the high external clock field in X-axis. In second clock state the next 4 magnet is activated with high field, while
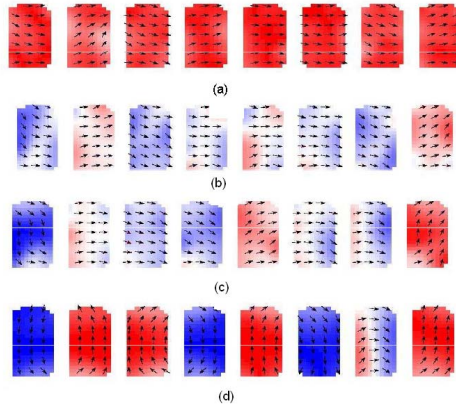
Figure 4.3 Conventional clock (Alam *et.al*) : Simulation result for 8 nanomagnet rectangle shape MCA array: (a) clock field in hard axis is applied to make all the nanomagnet null. (b) release the clock filed adiabatically and input is applied to the left most nanomagnet. (c) the first and last nanomagnet has strong magnetization during releasing hard axis field, hence output also start driving input. (d) not aligned correctly, frustration at 2 & 3 and 7 & 8 nanomagnet due to the bidirectional flow of information.

the field is released simultaneously from all the magnets in the first part. We could not reach ground state, causing incorrect result as shown in Fig. 4.4

We realized that as long as we have more than one magnet in a releasing field, clock state as opposed to the high external field, clock state (any number of magnet can be placed) , the input output directional information flow is not valid, as not only the input would be driving the output, but output will have impact over the input making the information reversible. As shown in Fig. 4.3 (B)(c) , output (right most) nanomagnet is stronger in polarization and influencing the driver.

The observation led us to design the true spatial Landauer clocking where each releasing clock state would have only one nanomagnet and the clock appears moving from input to the output deriving the directional aspect of conventional logic which is explained in next section.
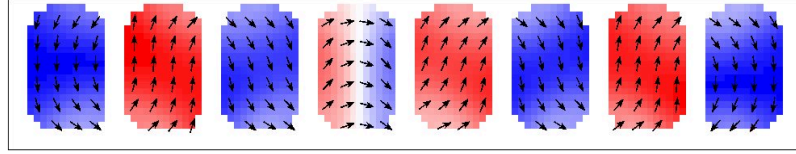
Figure 4.4 8 nanomagnet chain using neimier clocking scheme : frustration at the center causing incorrect logic at output

4.3 Spatially Moving Landauer Clocking Scheme

We propose a novel clocking scheme for Magnetic Cellular Automata where in essence, we deliver a spatially varying field from input to the output. The information processing in our scheme requires the interaction of the following three fields:

- *Null field*: It is the strong field applied to the hard axis (X-axis) of the nanomagnet, resulting in the Null clock state which holds no binary information ('1' or '0'). A large group of nanomagnets can be placed in null clock state.

- *Switching field*: It is reduced hard axis (X-axis) field, resulting in switching clock state in which the nanomagnet state is solely determined by its previous neighbor. There is only one nanomagnet in switching clock state.

- *Input field*: It is the small biased field given to the input nanomagnet in Y-axis to propagate the information down the line.

In this scheme, we drive all the cells initially to null state (hard axis) and then we decrease the field of the input nanomagnet to switching field while the remaining nanomagnets are at null state. In the next time slot we decrease the field of next nanomagnet while rest are still at null state and so on, thereby removing field from the nanomagnet cells one by one.

Fig. 4.5 illustrates, in more detail the Landauer clocking scheme for MCA. The figure shows an MCA array, implemented with 5 nanomagnets. The geometry of nanomag-
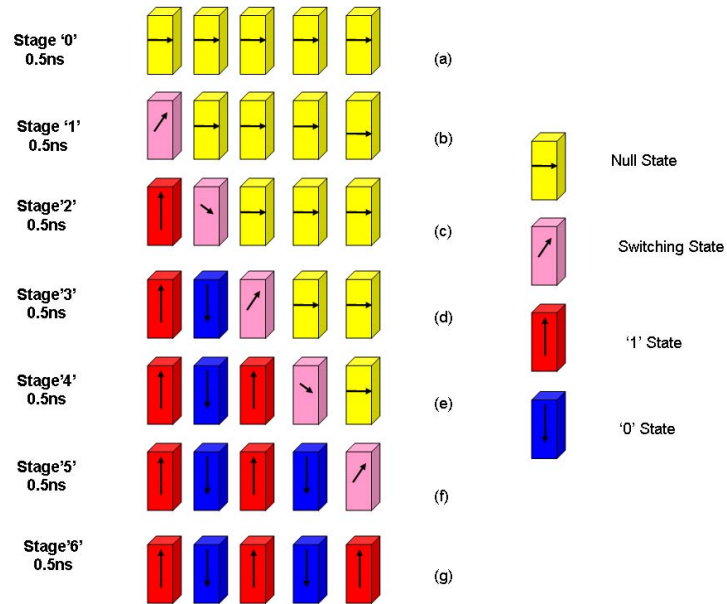
Figure 4.5 Landauer clocking: Showing 7 stages for 5 nanomagnet chain. Yellow color shows the null state, Pink color is for switching state, Red '1' and '0' for Blue . Each stage is for 0.5ns: (a) Null state, all the nanomagnets in the array forced in hard (x-axis) axis. (b) The Null-field from the left most nanomagnet is moved, comes under the switching field, at this time input '1' is given. (c) Null-field from the second nanomagnet is moved, and comes under the influence of switching field while remaining nanomagnets are at Null-field. (d) The second nanomagnet attained the stable state according to the previous neighbor (1st nanomagnet) and a third nanomagnet comes under the switching-field.
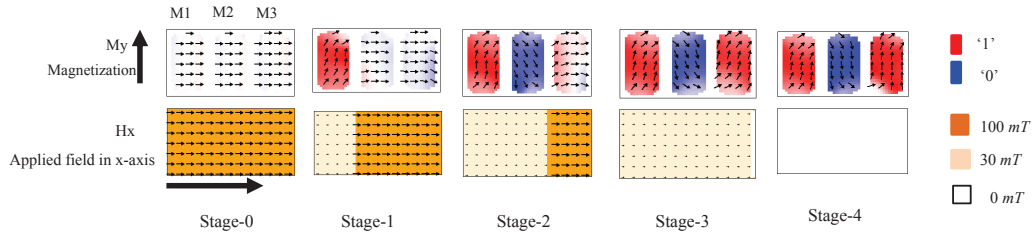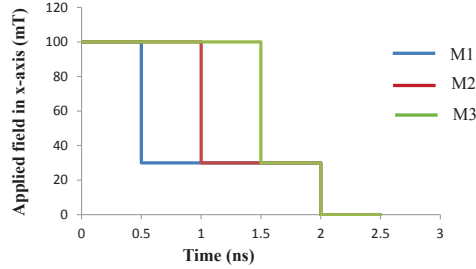
Figure 4.6 (a) Different stages of 3 nanomagnet wire. (b) The applied field in x-axis with respect to time for 3 nanomagnet wire namely, M1, M2 and M3.

nets allows three distinct states of magnetic polarization, which depends on the strength of magnetic field applied to the cell. Fig. 4.5 illustrates the snapshots of the circuit at different stages as it is clocked using the Landauer clocking scheme. We are giving input to the left most nanomagnet of MCA array and the output signal propagate to the right of the MCA array. The flow of information across the array is controlled by the clocking signal. The purpose of clocking field is to gradually drive the nanomagnets in a particular state, from null to active state.

The active state is determined by the state of the neighbor nanomagnet. In this clocking scheme initially all the nanomagnets are in stable anti-parallel state. All the nanomagnets then drive into null state by null clocking field in hard axis (X-axis) as shown in Fig. 4.5 (a). Then we move the strong null field from the left most nanomagnet, and

44

give the small switching field in hard axis, which brings it into switching state, and at this point input field is given as shown in Fig. 4.5 (b), while the rest nanomagnets remain at null state. Now clock field is moved from next magnet and it comes into the influence of switching field and hence it moves into the stable state (magnetization in Y-axis) as shown in Fig. 4.5 (c). The nanomagnet in switching state is influenced by the stable state of the previous nanomagnet as opposed to the following nanomagnet, which is in null state. This is because the magnetization of the null state nanomagnet is in X-axis. In this manner the null field is removed from all the nanomagnets, resulting in directional information flow from input to output as shown in Fig. 4.5 (d), (e), (f) and (g).

We employed spin dynamics and Landau-Lifshitz-Gilbert equation, which is packeted in OOMMF code to obtain time evolution. We wrote the script for spatially varying field using embedded function Oxs_StageZeeman.

Our main focus is to study Landauer clocking schemes with soft permalloy(80-20) magnetic interconnects under various design scenario. And the parameters values used for the numerical calculations were Ms = 8.5e5 , A = 13e-12 and K = 5.0e2. We study the required clocking field strength and switching field strength varying primarily three parameters aspect ratio, shape and scaling. The optimized design of interconnects was validated for 8, 16 and 32 length magnetic array. The design space was explored sequentially:

- First, we varied the aspect ratio for two shapes (rectangle and oval). It has to be noted that various shapes has been studied earlier [60] and their reliability has been studied. In this work, we resorted to basic shapes commonly used for proof of concept [61] to validate our clock. Similar study can be extended for other shapes. We found that for some aspect ratios, the system of interconnect does not align anti-ferromagnetically and for some others, it required large clock

energy. Based on our observation, 60 x 90 x 20nm rectangular shape magnetic interconnect has best promise in terms of lower clock and switching energy requirements.

- We also studied the input bias and simulation results show uniform input bias for both Oval and rectangles with optimized aspect ratios.

- Next, we observe that clocking field not depend on length of the nanomagnet array for Landauer clocking as opposed to [6] where larger length array were not reaching the ground state properly.

- Finally, we scale the 60 x 90 x 20nm rectangular shape magnetic interconnect (since this configuration yielded the lowest clocking field requirement) with scaling factors 0.8, 0.6 and 0.4 and we observe that clocking field required linearly reduces with scaling. This matches with the clocking energy projection by [6].

4.3.1 Aspect Ratio and Shape

It is already demonstrated that the reliability of coupling between nanomagnets is shape dependent [61]. The shape anisotropy is related with the geometry of nanomagnets, which is given by

$$H_{SA} = d \sum_j S_j^2 \tag{4.1}$$

Where d is the constant (related to the aspect ratio) and S_j is the magnetic moment of the jth cell. Shape anisotropy is present due to the dipolar interaction between the individual spin within the nanomagnet [62]. We looked into the four different aspect ratios 0.4, 0.5, 0.66, 0.8, utilizing Landauer clock. From our simulation results we found out that shape anisotropy is not only important for reliability of coupling

(a)

(b)

Figure 4.7 Simulated MCA array of 60 x 90 x 20 nm: (a) rectangle shape 8 nanomagnet array and (b) oval shaped 8 nanomagnet array.

(a)

(b)

Figure 4.8 Simulated MCA array of 50 x 100 x 20 nm: (a) rectangle shape 8 nanomagnet array and (b) oval shaped 8 nanomagnet array.

between nanomagnets, but it plays a significant role in clock field strength also. It has been proved that very low aspect ratio requires very high external field due to high coercive field. If we take high aspect ratio i.e. the more square like structure with smaller coercive field, it prevents magnetic arrays being used for magnetic logic devices [60].

The nanomagnet array of size 60 x 90 x 20nm (aspect ratio 0.6) requires less null field (70mT) for both shapes rectangular and oval as compared the size 50 x 100 x20nm and 40 x 100 x 20nm array. It is depicted from the Table.4.1 that for rectangle shape, the null field required for aspect ratio 0.4 is more than twice (150mT) than for aspect ratio 0.6 and for aspect ratio 0.5 it is 40mT more than that for aspect ratio 0.6. The oval

(a)

(b)
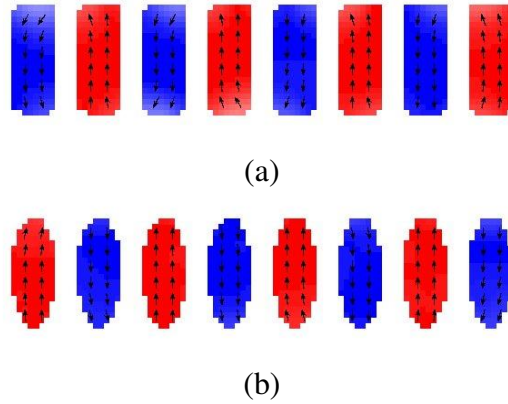
Figure 4.9 Simulated MCA array of 40 x 100 x 20 nm: (a) rectangle shape 8 nanomagnet array and (b) oval shaped 8 nanomagnet array.
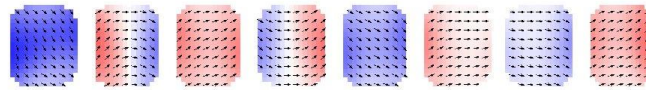
Figure 4.10 8 nanomagnet rectangle shape MCA array with aspect ratio 0.8 ($72x90x20\ nm$).

(angular) shape with aspect ratio 0.4 and 0.5 required high null field because of strong demagnetization field (shape anisotropy). The shape anisotropy require high null field because the energy difference between the two states is dependent on the shape and size of the nanomagnet [61]. Table4.2 shows that oval shape of aspect ratio 0.4 required null field three times more than that for aspect ratio 0.6 and more than twice that for aspect ratio 0.5. Hence in general oval shape and low aspect ratio requires high null field. Figure 4.7, 4.9 and 4.8 shows the simulated result for 0.6, 0.5 and 0.4 aspect ratio of 8 nanomagnet MCA array.

We have also noticed that high aspect ratio (0.8), having square like structure didn't work. It did not attained ground state as shown in Figure 4.10.

Table 4.1 Field requirement for rectangular shape nanomagnet chain.

$Aspect-ratio$	$Null-Field\ (mT)$	$Switch-Filed\ (mT)$	$Input-Field\ (mT)$
0.4	150	40	3
0.5	100	30	5
0.6	70	20	5

Table 4.2 Field requirement for oval shape nanomagnet chain.

$Aspect-ratio$	$Null-Field\ (mT)$	$Switch-Filed\ (mT)$	$Input-Field\ (mT)$
0.4	170	50	3
0.5	130	40	5
0.6	70	20	5

The switch field is less than the null field as shown in Table4.2. We have seen similar trend, the Oval shape requiring high switch field which decreases with increase in aspect ratio as shown in Table4.2. The 0.6 aspect ratio require less switch field ($20\ mT$) as compared to the 0.5 and 0.4 aspect ratio.

Through our simulation results we have shown that input field required is very low and is same for aspect ratio 0.5, 0.66 ($5\ mT$) irrespective of the shape as shown in Table4.1 and Table4.2. While the input field required for low aspect ratio 0.4 is less ($3\ mT$) than the other two aspect ratio as shown in Table4.1.

49
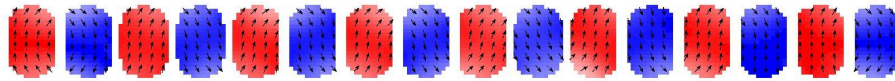
(a)
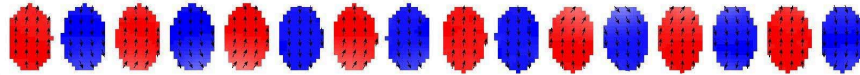
(b)

Figure 4.11 Simulated MCA array of 60 x 90 x 20 nm: (a) rectangle shape 16 nanomagnet array (b) oval shaped 16 nanomagnet array.
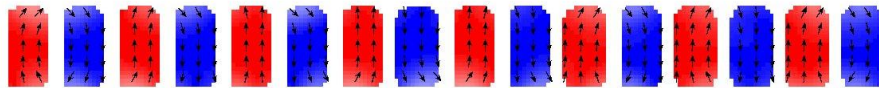
(a)
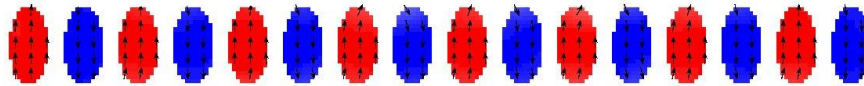
(b)

Figure 4.12 Simulated MCA array of 50 x 100 x 20 nm: (a) rectangle shape 16 nanomagnet array (b) oval shaped 16 nanomagnet array.
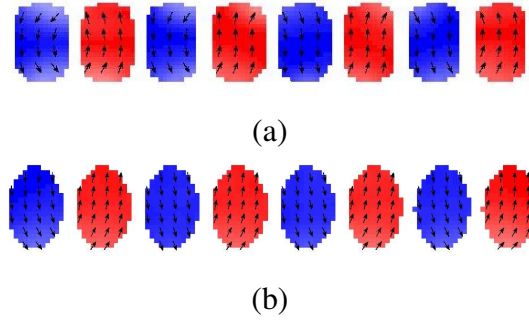

(a)
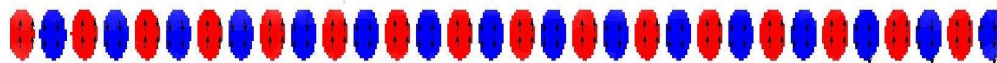
(b)

Figure 4.13 Simulated MCA array of 60 x 90 x 20 nm: (a) rectangle shape 32 nanomagnet array (b) oval shaped 32 nanomagnet array.

(a)

(b)

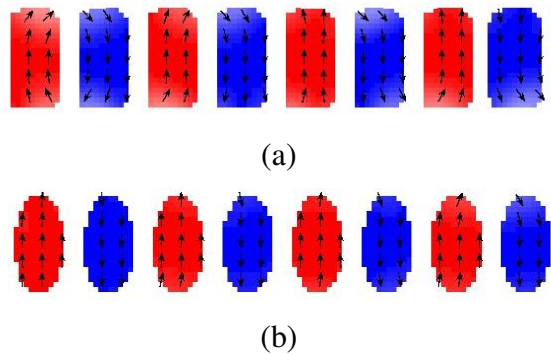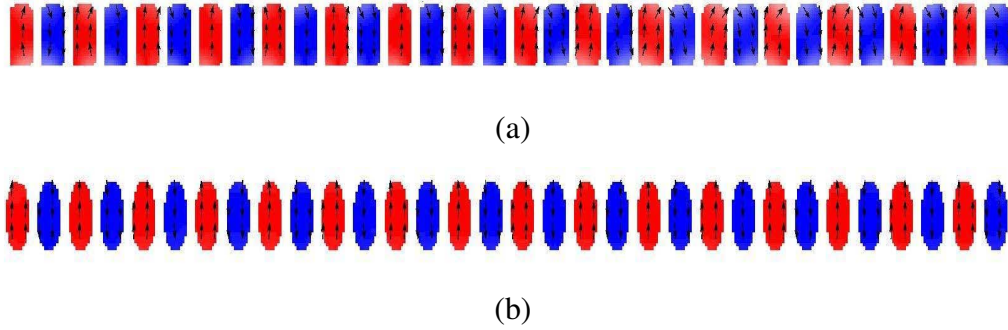Figure 4.14 Simulated MCA array of 50 x 100 x 20nm: (a) rectangle shape 32 nanomagnet array (b) oval shaped 32 nanomagnet array.

4.3.2 Length of Nano-magnets

We also did the clock study on three different array lengths (8, 16, 32). The clock field required for 60 x 90 x 20 nm nanomagnet array of 8, 16 and 32 elements is 70 *mT* null field, 20 *mT* switch field and input field is 5 *mT*. The Figure 4.11 and 4.13 shows simulated result for 16 and 32 nanomagnet MCA interconnect array. For 50 x 100*x*20 *nm* MCA array the field required for correct evaluation is 100 *mT* null field, 30 *mT* switch field for rectangle shape and for oval shape, 130 *mT* null field, 40 *mT* switch field is required which is same for all length arrays (8, 16, 32). Figure 4.12 and Figure 4.14 shows the simulated result for 16 and 32 nanomagnet MCA array for 0.5 aspect ratio. So in general the MCA array length doesn't matter with regards to the clock field strength.

4.3.3 Scaling

From the shape anisotropy study, we concluded that rectangular shape is best for the MCA architecture, as it required less clock field strength as opposed to oval shape. We conceive our next study i.e. scaling of nanomagnet, with the rectangular shape and 60*x*90*x*20 *nm* (0.6 AR) size nanomagnet MCA array. It has been demonstrated that MQCA based logics are scalable [63]. We have scaled the MCA array with different

Table 4.3 Field requirement for oval shape nanomagnet chain.

$Scaling\ factor$	$Null-Field\ (mT)$	$Switch-Filed\ (mT)$
0.8	50	15
0.6	30	5
0.4	20	5

factors and observed that clock field strength decreases with scaling as explained in Table 4.3. This is because as we scale down the size of nanomagnet array the surface volume of the nanomagnet decreases, resulting in small magnetization hence requiring less clock field to re-evaluate the array.

4.4   Discussion

we have demonstrated the novel Landauer clock for MCA array. We have studied the feasibility of spatially moving clock field by using the micro-magnetic simulator. To summarize few important features of proposed spatially moving clock scheme:

- Landauer clock has directional flow of information from input to output, as output has no impact on driver (input), unlike conventional adiabatic clock.

- Our Landauer clock is not similar to Landauer phase clock used for molecular QCA, in which after every fourth cycle first phase repeats [64] [65].

- The Landauer clock implies that in every clock zone there should be one nanomagnet rather than a group of nanomagnets.

- Clock field is invariant with length (8, 16, 32) and works perfectly all the time, yielding anti-parallel cell.

- Oval shape nanomagnet requires high clock field strength as compared to rectangular shape nanomagnet. Hence it is not suitable for MCA architecture.

- Input field required is very low and is same for both shapes (rectangle and oval) for optimized aspect ratio.

- Clock field decreases linearly with scaling of nanomagnet.

- More than one nanomagnet in one clock zone didn't result in ground state (anti-parallel).

CHAPTER 5

DEFECT ANALYSIS IN MCA ARRAY

The chapter will focus on the conventional electron beam lithography fabrication defects, which results in non-uniform cell structures.The simulation based study on their effects on information propagation in a wire is presented. The study varies the location of the different types of defects throughout the MCA wire under the influence of a spatial moving clocking field.

5.1 Defect Study

To accurately capture the reliability effects, defects have on a MCA system it is necessary to have a working clock. Regardless of the implementation, a circuit or system made from Cellular Automata devices will realistically require some kind of clock structure that directs the computation and provides gain. Since magnetic interactions are direction-insensitive, additional control (clock) is needed apart from an input to drive the information flow from input to output. The clock helps the system to overcome the energy barriers between metastable states and the ground state.

E-QCA defect characterization has been extensively studied [66][67], however very little work has been reported on MCA defect characterization. The main focus of this paper is on the defect characterization of magnetic cellular automata wire under a working clock. There are two preliminary defect studies under conventional adiabatic

ordering scheme [68][52]. Both studies are not comprehensive, since defect masking towards the output (point of testing) could not be considered as perfect ordering. This study assumes a functionally correct array with perfect ordering and the flow of information [53], while in [68][52] the defect free order was itself in question. It is important to note that, the actual implementation can vary [69] but as long as ordering is correct, the defect characterization conducted in this work would remain valid. Since the functional ordering was achieved by spatially varying field implemented by script on OOMMF package, this study includes a large category of single cell defect. Moreover all our defect data and ground truth (probability of defect) are found from in-house fabrication experience as opposed to the common defect assumption.

5.2 Types of Fabrication Defects

In our Nano Research Center [70], we have successfully fabricated MCA arrays of various lengths. The process begins with the coating of resist (PMMA) on Si wafer, which is followed by lithography. We have used electron beam nano-lithography (JEOL SEM 840) with a high yield and NPGS system [71] to write the patterns on the resist, afterwards we deposited the ferromagnetic material of our choice, in this case permalloy, via the Varian Model 980-2462 Electron Beam Evaporator. We achieve a vacuum of about 2μ Torr and evaporated the material, after that we processed the lift-off to fabricate nano size magnets, with a considerable height and a good surface quality.

Figure 5.2(a) shows a defect free array, act as wire of 20 nm thick permalloy nanomagnets. Our main focus in this paper is to characterize the defects in MCA array, which we have seen in our experiments as shown in Figure 5.2(a), (b), (c), (d), (e), (f). When feature sizes in a device are small enough, the fabrication defects in nano-fabrication

(a)   (b)

(c)   (d)
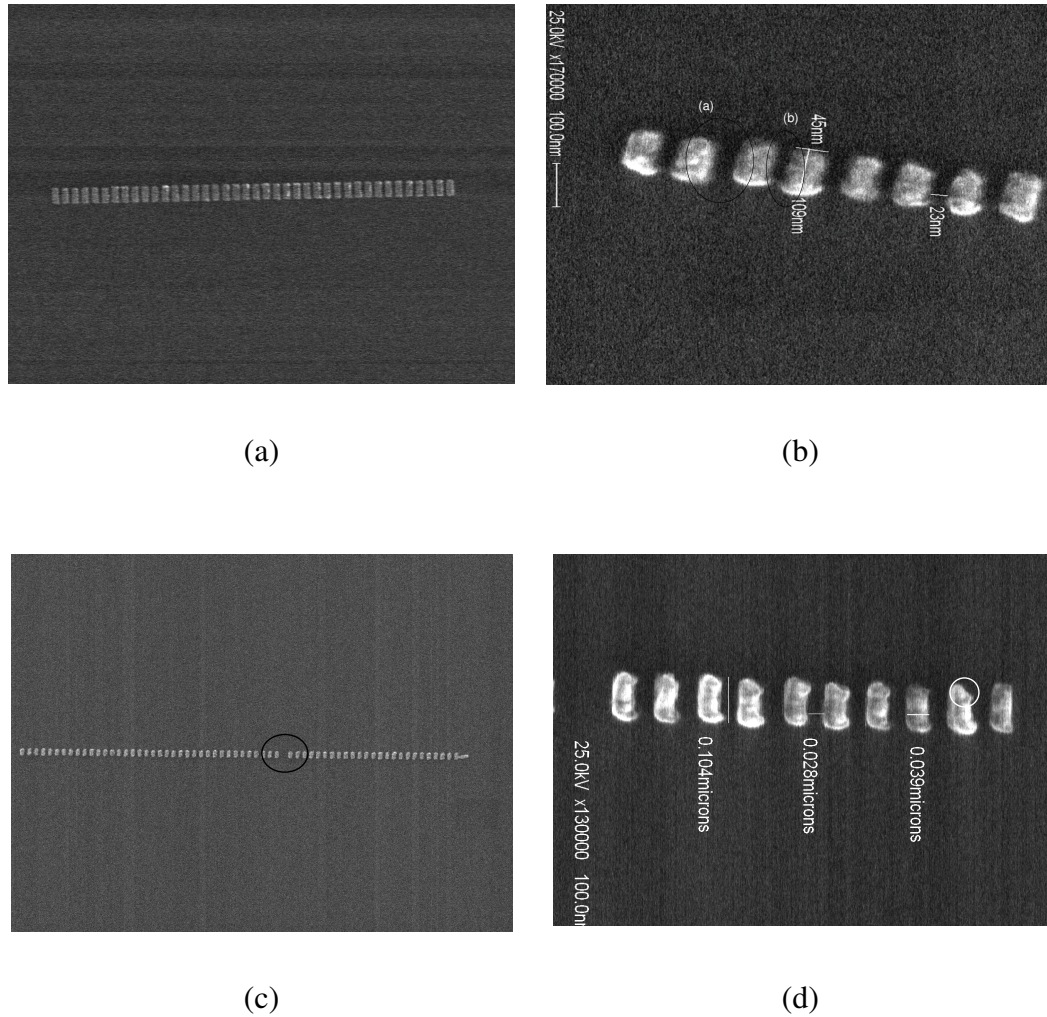
Figure 5.1 (a) An ideal chain, where the shape of the cells is regular. As a result the single domain dipole moments are strongly coupled. (b) Irregular spacing between nanomagnets (A) Large spacing (B) Small spacing. This can be due to blanking or deflection errors which may occur when the electron beam is not deflected properly when it is supposed to or due to shaping errors which occur in variable-shaped beam systems. (c) Missing cell in an array, which may be due to unexposed of the resist caused by contamination of the resist. (d) Missing material defect (electrons from exposure of an adjacent region spill over into the exposure of the currently written feature, effectively enlarging its image result in merging).

(a)   (b)
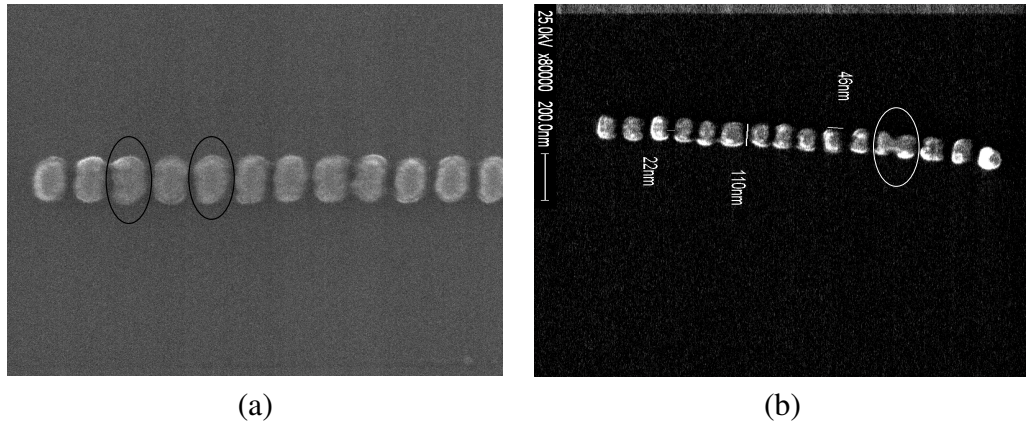
Figure 5.2 (a) Bulge defect seen in nanomagnet array and (b) Partial merge magnet in MCA array (electrons from exposure of an adjacent region spill over into the exposure of the currently written feature, effectively enlarging its image result in merging).
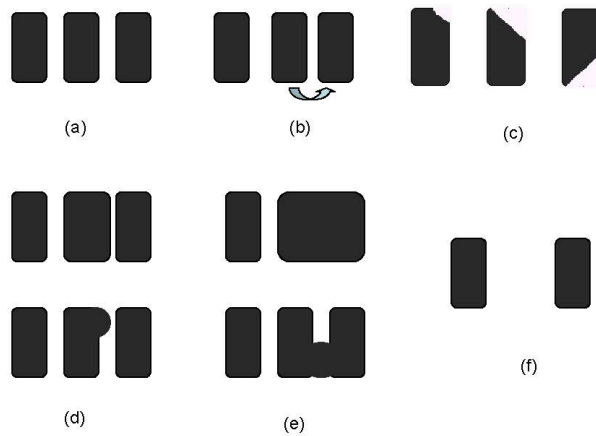
Figure 5.3 Type of defect characterized (a) Defect free nanomagnets (base case) all the nanomagnets are of regular shape (50 x 100 x 20 nm^3) with 20 nm uniform spacing between two nanomagnets, (b) Irregular spacing, two nanomagnet (2 and 3) comes close and other nanomagnet (magnet 1) moved farther apart, (c) Missing material defects with different amount of missing material and from different location (top/bottom) in nanomagnet, (d) Bulge defect with two form namely, uniform bulge (upper array) which results in an increase in the width of the 2nd nanomagnet and non uniform bulge (bottom array) which results in the bump at the top of the 2nd nanomagnet, (e) Merge defect with two types, first fully merged cell as shown in upper array, magnet 2 and 3 merged completely and second is the partially merged cell (lower array) and (f) Missing cell defect, in which whole nanomagnet (2nd) is missed.

57

methods can become a dominant factor which determine the actual shape and operation of the nano-structure. The cause of these defects can be extrinsic or intrinsic [72]. We have noticed during our fabrication that defects may be possible in the writing phase, in which the pattern is transferred on the resist, and the deposition phase, in which nanomagnets are deposited on the substrate. The cause of defects can be sample charging (either negative or positive), backscattering calculation errors, dose errors, fogging (long-range reflection of backscattered electrons), out-gassing, contamination, beam drift and particles [73]. The essence of the observed defects in Figure 5.2 are categorized into the following groups:

- *Defect Free*: all the nanomagnets are of regular shape of dimensions 50 x 100 x 20 nm^3 and optimum space of 20 nm between nanomagnets, as shown in Figure 5.3(a).

- *Irregular spacing*: the spacing between nanomagnets is not uniform (observed regularly). It is clear from the Figure 5.3(b) that two regular shaped nanomagnets (2 and 3) come closer which causes increase in the spacing between nanomagnets 1 and 2. In our experiments we have noticed that space irregularity is very common in MCA array.

- *Missing material*: some portion of the particular nanomagnet is missing as compared to the original (defect free) arrangement as shown in Figure 5.3(c). In order to study missing material defect, we have considered two cases (1) Different amount of missing material as shown in Figure 5.3(c) where 1st nanomagnet has less missing material as compared to the 2nd and 3rd nanomagnet (2) Different locations (top/bottom) of missing material in nanomagnet as shown in Figure 5.3(c).

- *Bulge magnet*: (a) uniform bulging in nanomagnet results in a big nanomagnet which in turn decreases the spacing between two nanomagnets and hence also leads to irregular spacing as shown in Figure 5.3(d), top array (2nd magnet is bulged) (b) non-uniform bulge, in which there is an increase in the magnetic material which looks like bump as shown in Figure 5.3(d), bottom array. Note that all bulge defects are frequently observed.

- *Merged Magnet*: Individual nanomagnet merge with the neighboring nanomagnet as shown in Figure 5.3(e). Further classifications are (a) fully merged cell, where two nanomagnets merge completely and form one big nanomagnet as shown in Figure 5.3(e), top array (b) partially merged cell, in which portion of the near-by two nanomagnets merge as shown in Figure 5.3(e), bottom array.

- *Missing cell*: entire cell is missing (rarely occurring) as shown in Figure 5.3(f).

In this framework, we have studied the geometry defect, which occurred during fabrication process. The geometry defects are deterministic in nature unlike the soft temporal error arising out of noise, stray magnetic field and temperature variations. The scope of the current study is (1) single occurrence of each defect type in an array and (2) assumption that input-output nanomagnets are defect free.

In our study, we have assumed room temperature operation (T=300K) and neglecting thermal fluctuations. Furthermore, the impact of stray noise and thermal fluctuation would be minimal at the dimensions of our study (as the ground state energy of the magnets under study (100 x 50 x 20 nm^3) are a few orders of magnitude of kT at room temperature [46]).

Also, in our study surface roughness is neglected and we have assumed the uniform crystalline structure.In this framework OOMMF tool by NIST has been used. The OOMMF has great convergence with quantitative SEMPA measurements.

5.3 Defect Analysis

We analyze the magnetic cells using Landau-Lifshitz equation (micro-magnetic the-
ory) which accounts for various energies like Zeeman energy, Magneto-static energy,
Exchange energy, Anisotropy energy, Demagnetization energy to model the behavior
of the defective array. This framework presents an extensive and thorough defect study
of realistic fabrication defects. Because of the nano scale size magnet and inherent
noise of electron beam lithography, the type of defect observed in fabrication process
are 1) less frequent missing cell 2) minimum fully merge cell and 3) missing material,
bulging and irregular spacing defects which occur commonly.

5.3.1   Micro-magnetic Simulation Parameters

We performed the micro-magnetic simulation using the OOMMF code, based on the
Landau-Lifshitz equation. The program approximates the continuum micro-magnetic
theory, where the magnetic sample was divided into a regular two dimensional grid
of square cells. Within each cell, the magnetization is assumed to be uniform and is
represented by a three dimensional spin vector M. The exchange energy is computed
via eight-neighbor scheme [74], while the magneto-static energy is calculated via a
fast Fourier convolution of the magnetization. The dimension for nanomagnets used
for this analysis is 50 x 100 x 20 nm^3, and spacing between nanomagnets is 20 nm.
A unit cell size of 5 nm was used for the simulations. The parameter values used for
the numerical calculations were characteristic of permalloy (Ms = $85x10^5$ A/m, A =
$1.3x10^{-12}$ J/m, K =$500J/m^3$).

We commence this section by explaining the simulation process, wherein we have
considered an array of 8 nanomagnets and 16 nanomagnets of MCA. In this frame of
work, we have used a spatially moving clock scheme [53] for defect analysis in MCA

60
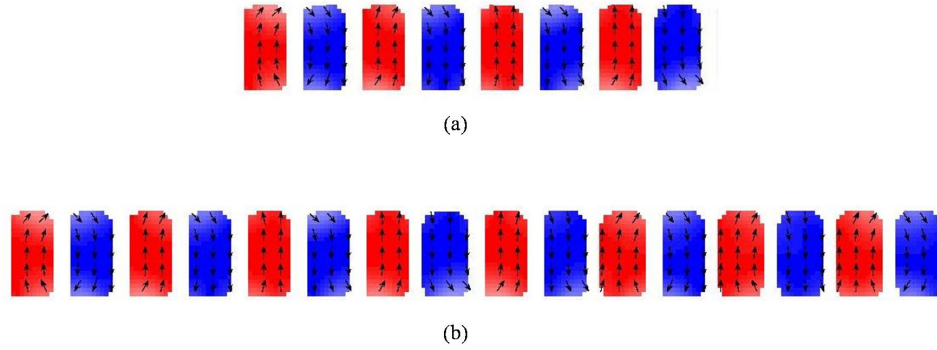
Figure 5.4 Defect free nanomagnet array: (a) 8 nanomagnet MCA array and (b) 16 nanomagnet MCA array.

architecture, where we deliver a spatially moving clock from input to output. The information processing requires the interaction of the three fields: null field, switching field and input field. In this, the null field (clock) of 100 mT along the hard-axis (in x direction) was applied which forced all the magnetic cell moments to align in the direction of field (hard-axis) and magnetization in easy-axis reached zero. As we vary field spatially, the nanomagnets come under the influence of switching field (30 mT) and finally start aligning anti-ferromagnetically, according to the input magnetization. The propagation happens primarily due to the neighboring cell exchange coupling and shape-anisotropy. The simulation result in Figure 5.4, under no defect, shows that magnetic arrays behave perfectly, reaching near-uniform magnetization of individual cells, arranged in perfect anti-ferromagnetic order.

5.3.2   Single Irregular Spacing Defect

This is the most noticeable fabrication defect. Here we want to clarify that this study is not meant to decide optimum spacing. We have concluded that 20 nm spacing is optimum for our magnet dimensions which also confers with the relative dimensions used by Csaba *et. al.*, [43]. In this work, we intend to study effect of a single regular shaped cell spaced irregularly due to fabrication variations (caused by effects like

61
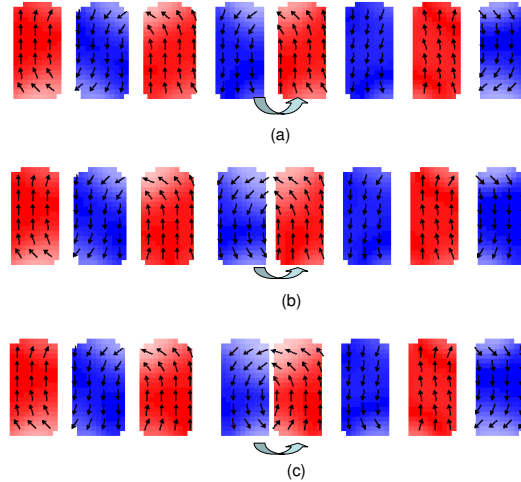
Figure 5.5 Irregular spacing defect in 8 nanomagnets: (a) Irregular space (5 nm) between nanomagnets 4 and 5, (b) Irregular spacing of 10 nm and (c) Irregular space between nanomagnets 4 and 5 of 15 nm, all defects are masked.

stray magnetic fields, thermal fluctuations, contaminated resist etc.) common in litho-based assembly. We need a robust architecture that would be tolerant to small spacing irregularities.

Figure 5.5 shows, nanomagnets 4 and 5 spaced irregularly. Irregular space defect has been studied with conventional clock [68], wherein the irregularity in space cause stuck-at-fault. However our analysis suggested that irregular spacing does not affect the functionality of the MCA array. In Figure 5.5, MCA array of 8 nanomagnet is simulated with different space irregularities (25%, 50%, 75%) and observed that MCA arrays are more tolerant against irregular space defects.

5.3.3 Missing Material Defect

We have characterized the missing material defect in two different forms, namely (1) Different amount of missing material and (2) Different location (top/bottom) of missing material in MCA arrays.
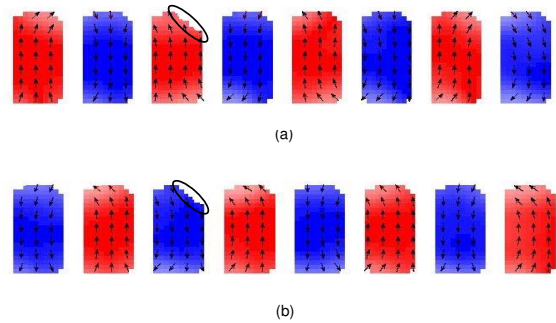
Figure 5.6 Missing material less than 5% in 3rd nanomagnet in 8 nanomagnet array, gives correct output.
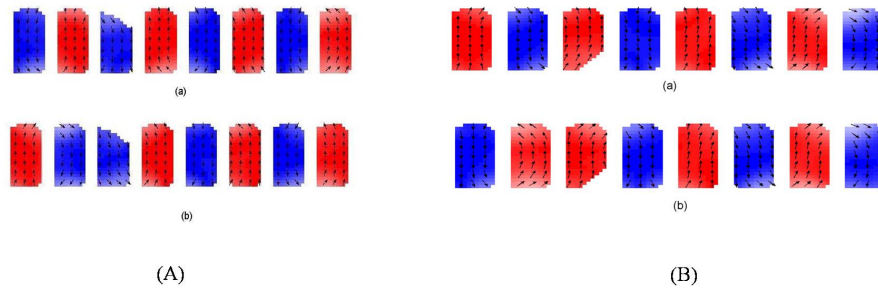
Figure 5.7 (A) Missing material with large amount from top of the 3rd nanomagnet; (a) logic zero propagate correctly (b) logic one does not propagate correctly as the 3rd nanomagnet did not flip and retains old value. (B) Missing material from bottom of the 3rd nanomagnet.

First set of simulations dealt with the small amount of missing material defect. The 8 nanomagnet MCA array was considered and 5% of material from top of the nano-magnet was removed as shown in Figure 5.6. The array displayed perfect logics ('1' and '0') with small material loss. Simulations were repeated again but now with the removal of high percentage of missing material (20%). Subsequently, we found that if the material is missing from the top, the magnetization is always downwards in the defective nanomagnet as shown in Figure 5.7 (A), whereas if the material is removed from the bottom, the magnetization is always upward (logic 1) as shown in Figure 5.7 (B). Shape anisotropy property of single domain nanomagnet plays an important role (as the perfect part has better defined shape as compared to the missing material part). As the percentage of missing material increased, it was difficult to null the nanomagnet, hence after removal of clock field the nanomagnet would retain the old value. Thus, the missing material more than 5% results in the stuck-at-0 or stuck-at-1 depending on the location of the missing material (top or bottom).

5.3.4 Single Bulge Defect

We have seen in our fabrication that the probability of occurrence of bulge in nano-magnet is very high due to unavoidable lithography variations. We have characterized the bulging defect in two scenarios as discussed in previous section. The study begins with the uniform bulging in nanomagnet resulting in increase in the width of the nano-magnet which causes the decrease in the spacing between the neighboring nanomagnet (left or right). Niemier *et.al.* have demonstrated the effect of bulged nanomagnet array with conventional clock and reported that bulging results in weaker 1 and 0. In this frame of work we have explored the bulge defect. We have assumed only one bulge defect in an array as shown in Figure 5.8.

	Normalized (My)
Input magnet	0.97
Bulge magnet (4th)	0.83
Output magnet	0.967

(A)   (B)
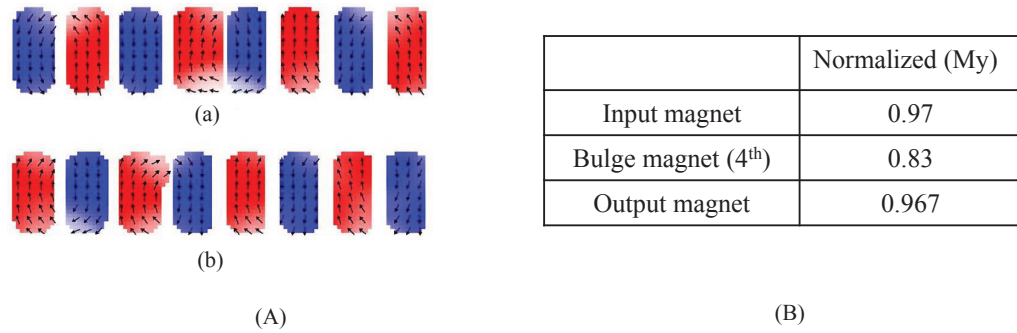
Figure 5.8 (A) Results for bulge defect in 8 nanomagnet array (a) uniform bulge at 4th nanomagnet (30% increase in the width of the nanomagnet) results in the decrease in the spacing between 4th and 5th nanomagnet, (b) non-uniform bulge at the 3rd nanomagnet (small bump at the top). (B) Normalized magnetization in nanomagnet.

We have simulated the 8 nanomagnet array with different percentages of bulge defects (10%, 20%, 30%). Figure 5.8 (A)(a) shows the results for 30% bulge (causing increase in width from 50 nm to 65 nm and decrease in spacing from 20 nm to 5 nm) in the nanomagnet. This is the maximum bulge in the nanomagnet because more bulge will result in the merging with the neighboring cell and cause merge cell defect which we will be discussing in following section. We have observed that magnetization in bulge nanomagnet (4th) is weak in Y-axis as shown in Figure 5.8 (B). However, the output magnetization is restored. Hence, due to shape anisotropy if the output nanomagnet is defect free, the bulge in the nanomagnet would not have any effect on the correct flow of information. Next we simulated the array with non-uniform bulging, commonly encountered in our fabrication experiments. Figure 5.8 (A)(b) shows the results for non-uniform bulge at $3^{r}d$ nanomagnet (top) in 8 an MCA array. The non-uniform bulge (at top of the 3rd nanomagnet) causes decrease in the space between nanomagnet 3 and 4 at the top. It is evident from the results that non-uniform bulging does not affect the correct flow of information as shown in Figure 5.8 (B) (b).
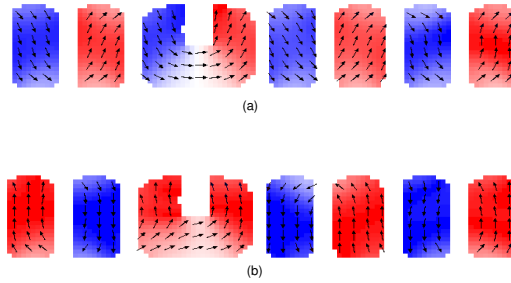
Figure 5.9 Partially merged cell defect in 8 nanomagnet array, nanomagnet 3 and 4 merged, (a) Initial state (b) Logic one cause error because the nanomagnet after merged cell does not flip and retains the old value.
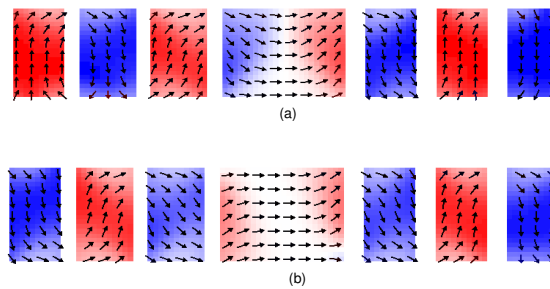
Figure 5.10 Merge cell defect in 8 nanomagnet array, nanomagnet 4 and 5 merged, (a) logic one propagates correctly but (b) logic zero cause error because the merged nanomagnet does not flip.

5.3.5 Merged Neighboring Cell Defect

We have seen two types of merge cell defect. First, the partial merge cell defect, in which portion of the near-by two nanomagnets are merged as shown in Figure 5.9. Second, the fully merged cell, where two nearby nanomagnets are merged completely (forming one big nanomagnet) as shown in Figure 5.10. We have simulated the effect of merge cell defect with spatially moving clock.

First set of simulations was run for partial merge cell defect. It is illustrated in Figure 5.9 that nanomagnet 3 and 4 partially merged, where Figure 5.9 (a) is the initial state (logic '0' propagation). We have applied the spatially moving clock in hard axis and input (logic '1') to the left most nanomagnet. The results shows that nanomagnet after the partial merge defect does not flip (retains the old value) which cause incorrect output as shown in Figure 5.9 (b).

The second set of simulation involves the Merge cell defect as shown in Figure 5.10 where nanomagnet 4 and 5 merged completely, which results in one big nanomagnet. Figure 5.10 (a) is the initial state (logic one propagation). We applied the clock in hard axis and input (logic zero) was applied to left most nanomagnet. The results shows that Merge cell defect causes incorrect output as shown in Figure 5.10 (b). This is due to the merge cell having more magnetization in the x-axis as compared to the y-axis, therefore it does not flip. The nanomagnet after merge cell retains the previous value. Hence array works well with one input (logic '0' or logic '1') depending on the initial state of the array.

5.3.6 Missing Cell Defect

A large number of missing cell study is performed in the context of E-QCA [66, 67]. In our fabrication experiments, we have seen some missing cell as shown in Figure 5.2(c)
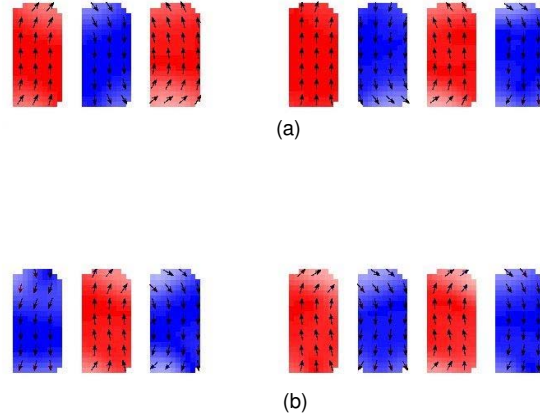
Figure 5.11 Missing nanomagnet in 8 nanomagnet array. (a) Logic one propagate and (b) Logic zero cause incorrect output.

in rare occasions. The MCA array behaves as decoupled arrays due to the large spacing created by the missing cell. MCA array with missing cell (4th nanomagnet) is shown in Figure 5.11. The initial state of MCA array with missing cell is illustrated by Figure 5.11(a). We have applied input to the left most nanomagnet and spatially moving clock in hard-axis of the nanomagnets. The input propagated correctly till 3rd nanomagnet and since 4th nanomagnet is missing, the 5th nanomagnet has no influence from the 3rd nanomagnet due to large spacing. Hence, the fifth nanomagnet will retain its old value as shown in Figure 5.11(b). So it will propagate either logic '1' or '0' depending on the initial state of the nanomagnet after the missing cell. Therefore, there is a 50% probability of getting correct output.

5.3.7   Role of Array Length in Defect

We have studied these defects with different array lengths. Figure 5.12 shows the non uniform bulge defect at 3rd nanomagnet in 8, 9, 10 and 16 nanomagnet MCA array. It is evident from the results that it is working perfectly irrespective of the length. This is
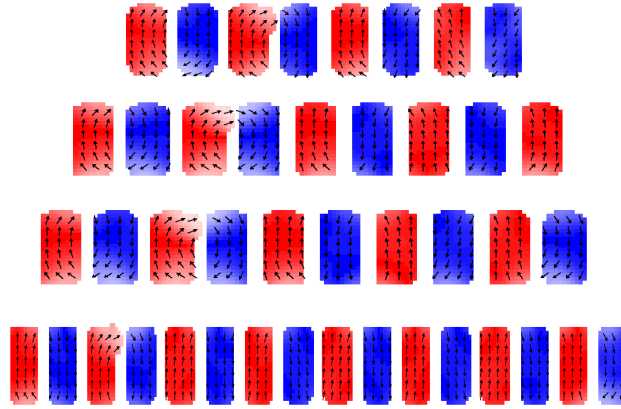
Figure 5.12 Bulge defect at nanomagnet 3 in 8, 9, 10, 16 nanomagnet MCA array.

a feature of spatially moving clock, where nanomagnet in switching state is influenced by the stable state of the previous nanomagnet as opposed to the following nanomagnet, which is in null state. This is because the magnetization of the null state nanomagnet is in X-axis. The null field is removed from all the nanomagnets one by one, resulting in directional information flow from input to output. Hence length is not a determinant in defect behavior.

5.3.8 Role of Location of Defects in Array

Here, we focus our attention on the effect of the defect location in MCA array. We have assumed that the input and output nanomagnets are defect free and there is a single irregular spacing defect in an array. Through our simulation experiments we observed that the location of defect in an array does not affect the correct propagation flow of information. The simulation results for irregular spacing defect in 16 MCA array at three different locations is shown in Figure 5.13.
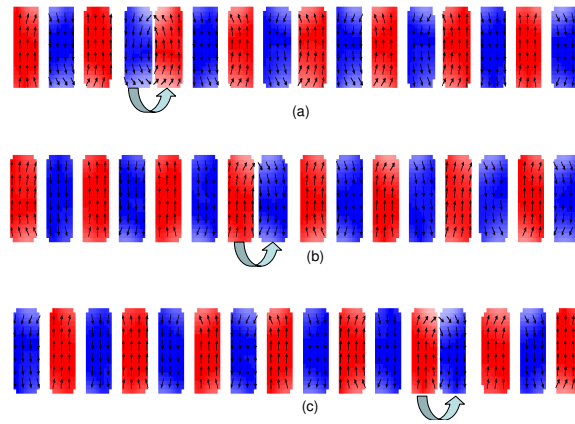
Figure 5.13 Irregular spacing defect in 16 nanomagnets: (a) Irregular space (5 nm) between nanomagnet 4 and 5, (b) Irregular spacing between nanomagnet 8 and 9 and (c) Irregular space between nanomagnet 12 and 13. All the defects are masked.

(a)

(b)
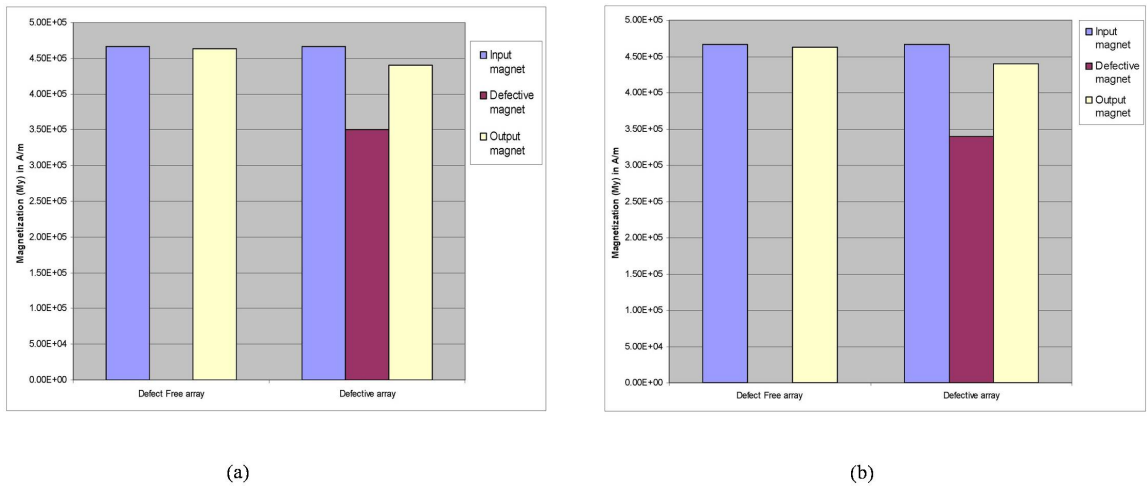
Figure 5.14 Measured output magnetization in nanomagnet array for (a) defect free and defective 8 MCA array and (b) defect free and defective 16 MCA array.

5.3.9 Output Magnetization under Defect

We have measured the input and output magnetization for the MCA array of length 8 and 16 nanomagnets as shown in Figure 5.14. It is evident from the Figure 5.14 that output magnetization strength is uniform for both the arrays. Next, for defective array (missing material defect), we observed that the magnetization of the defective nanomagnet is weak as shown in Figure 5.14 (maroon bar). However the defect in the array does not affect significantly the strength of the output magnet irrespective of the type of defect. This is no surprise to us as shape anisotropy in single domain nanomagnet is inherent to MCA architecture, which helps restore the magnetization of subsequent magnet. At this point, we introduce an index of defect-tolerance, R_D. This is the robustness with respect to the type of defect.

$$R_{D_i} = p(correct\ output | Defect_i\ has\ occurred)$$

It is clear from Table. 5.3.9 that Missing material defect (less than 5%), bulge nanomagnet defect and irregular space defect for array length 8 and 16, irrespective of the location of defect is extremely robust. Merge cell defect and Missing cell defect, which have less probability of occurrence have 50% chance of correct output. Hence the MCA architecture is more robust.

Table 5.1 Robustness measures for 9 and 16 MCA arrays with respect to various types of defect.

Defect type	R_{D_i}	
	8 nano-magnets	16 nano-magnets
Bulge defect	100%	100%
Missing material (less than 5%)	100%	100%
Missing cell	50%	50%
Merged cell	50%	50%
Irregular spacing	100%	100%

5.3.10 Discussion

The important points observed by our simulation experiments are summarized below:

- MCA systems are robust towards most of the defects (irregular spacing, bulge, missing material (5%)).

- The location of a defect in an array does not affect the defect masking.

- The stuck-at fault in missing material defect depends on the position of the missing material (top/bottom) in nanomagnet in MCA array, because in top missing material the magnetization in Y-axis is always downward while in bottom missing material the magnetization is always upwards.

- The stuck-at fault in a missing cell depends on the initial polarization of the MCA array. The nanomagnet after the missing cell does not have any effect from previous nanomagnet (due to large space created by missed cell), hence retains the old (initial) value.

72

- Also, stuck-at-faults in a merge cell depends on the initial polarization of the MCA array. In merged nanomagnet the magnetization in x-axis is more than y-axis so it is hard to flip the merged nanomagnet. Hence nanomagnet retains the old (initial) value which propagate either logic'0' or logic'1'.

5.4 Conclusion

We have studied the defect in MCA array for robustness of nanomagnetic arrays based on the theoretical framework of Landau-Lifshitz, capturing many effects like, shape anisotropy, crystalline anisotropy, exchange coupling between neighboring cells. First, we observed that with spatially varying clock scheme, length of an array and location of defect does not affect the output. Secondly, there was no signal degradation over the length of array and finally, we demonstrated that with spatially moving clock, MCA architecture is extremely robust to irregular space, bulge defect and missing material(less than 5%), which are ordinarily encountered in our fabrication experiments. Our future study include probabilistic defect macro-modeling.

CHAPTER 6

NANOMAGNET 2D ARRAY FOR COMPUTATION

6.1 Introduction

During the last five decade significant work have been devoted to the comprehension of the physical phenomena appearing in sub-micron size magnetic systems. The magnetic properties of periodic arrays of nanomagnet with deep sub-micron dimensions have an enormous technological impact, e.g. in the new generation of ultra-high density magnetic information storage devices, magnetic sensors. Besides, system of nanometric size posses an increasing importance in computing [75][76]. For high density devices to be competitive the nanomagnet have to be patterned in close proximity and therefore the studies focused on the effect of dipolar interaction between nanomagnets are of great current interest.

In order to implement the patterned nanostructure, an optimization of the geometry and size of small magnetic element is important. Many investigation is carried out so far on element with different geometrical details, such as in-plane aspect ratio (square Vs rectangular or circular vs elliptical), shape (rectangular, elliptical, triangular, square ring, circular, circular rings, pentagonal, etc) or thickness (disk like Vs.columnar) [77][78][79][80][81]. In recent years, there has been substantial work reported on the magnetic state of the single nanomagnet (single domain or vortex). Cowburn et.al [82] presented the phase plot, showing the transition between single domain state to vortex state as a function of thickness and diameter for single nanomag-

net. Also magnetic vortex has been studied extensively from various aspects, such as formation, detection and field/current induced dynamics. While these properties have been investigated in magnetic disk, rings and squares, the chirailty control has been attempted in the elements with elaborate design of introducing geometric asymmetry to the outer shape such as an edge-planed disk and ring [83][84].

Other than single nanomagnet study, there has been work done on the 1D array/chain and 2D array of nanomagnet. For instance natali et.al [85], guslienko et.al. [86] and Novosod et.al. [87] studied the 1D and 2D array of different element size, thickness and showed the change in magnetization reversal process in the system due to magnetostatic energy. Also cowburn et.al.[88] showed that by arranging the soft ferromagnetic element in linear array/chain and by engineering the anisotropy of each element, antiferromagnetic arrangement can be obtained. Previous work reported on properties of large area array (1D or 2D) of nanomagnets has been focused on the high density storage or media applications, where the structures sufficiently spaced to consider magnetostatic coupling between element negligible.in order to achieve minimum interaction between the elements, array of nanomagnet implemented with large thickness $(40 - 80\ nm)$ and diameter $(200 - 1500\ nm)$ that creates the vortex configuration of each nanomagnet, which results negligible neighboring interference. However, there has been no work reported so far on closely spaced nanomagnet array for computation. The key requirements to implement nanomagnet array for computation application are:

- Fast and reproducible operation, which is related with the magnetization reversal or switching process of the individual nanomagnet in the system. The single domain state with coherent (one step) reversal process is ideal for the computation, since it is associated with the shorter and sharp switching mechanism as oppose to the vortex state, where reversal takes places in more than one step including formation of nucleation.
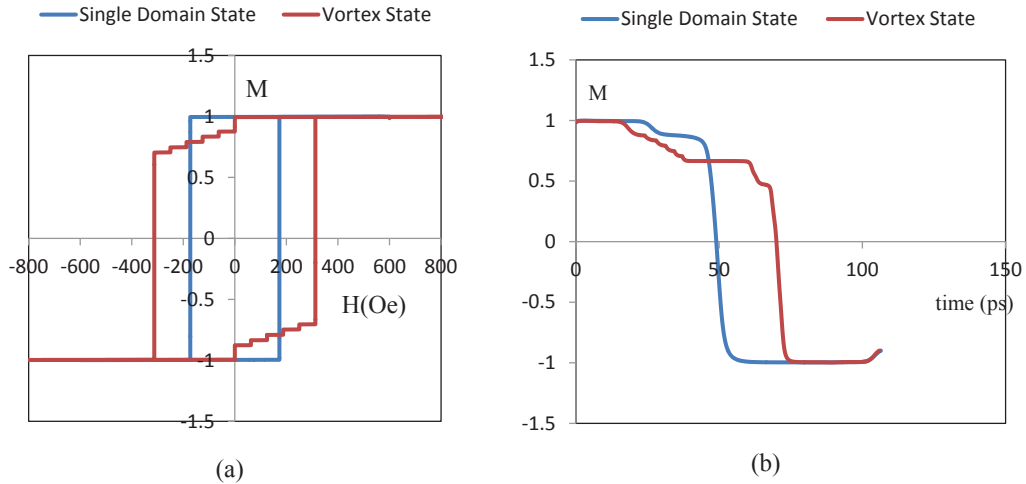
Figure 6.1 (a) Simulated hysteresis of 100 *nm* diameter with thickness 10 *nm* (having single domain state) and 15 *nm* (with vortex state) and (b) Magnetization of the nanomagnet.

- Dipole- dipole interaction, which is the main cause of the information flow in the nanomagnet. In order to enhance the dipole dipole interaction, the inter element spacing should be small (smaller than the element size), in contradict to high density storage application where nanomagnet array is design in such a fashion that there is no dipole-dipole interaction between neighboring nanomagnet. Furthermore, to exploit the dipole-dipole interaction, the individual nanomagnet should posses the single domain state due to high charge density at the edges of the nanomagnet which results strong dipolar field rather than vortex state, having no charge distribution around the edges and hence no dipolar field.

The single domain state has advantage of sharp one step switching over the vortex state, where reversal takes place through more than one step that includes the formation/creation of nucleation as predicted by the hysteresis. The fast operation is related to the short and sharp reversal as shown in the Fig.6.1. The nanomagnet with single domain state has sharp reversal as shown in Figure 6.1 (a) and switching takes place at 45 *ps* as shown in the Figure 6.1 (b). On the other hand nanomagnet with vortex state

76
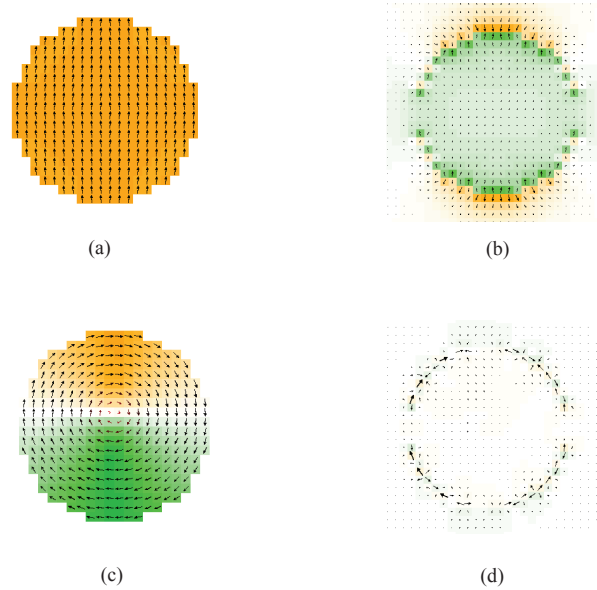
Figure 6.2 (a) Magnetization distribution in single domaim state, (b) Demagnetization field in single domain state, (c) Magnetization distribution in vortex state and (d) Demagnetization field in vortex state.

has 2 step reversal (nucleation formation) and switching takes place at 70 *ps* as shown in Figure 6.1. Hence the nanomagnet having single domain state with one step reversal has fast switching as opposed to the vortex state. As it evident from the hysteresis curve, shown in the Figure 6.1, the one step reversal constitute the fast operation.

In this work we report the theoretical numerical simulation studies of the magnetization state in 2D array of soft ferromagnetic sub-micron circular nanomagnet with variable diameter, thickness and small inter-element distance. As per our knowledge, there is no result available on the 2D array for the computation, with very small and equal spacing (20nm) along the both axis. It will be demonstrated that the magnetostatic inter-element interaction has a strong destabilizing effect on magnetization state. The numerical simulation study show that the magnetic state of the system strongly depend on the inter element distance, thickness and the size of array.

6.2 Micromagnetic Model

The micromagnetic simulations were carried out by solving the Landau-Lifshitz-Gilbert (LLG) equations, using the micromagnetic software [89] [90].

$$\frac{d\mathbf{M}}{dt} = -\gamma \mathbf{M} \times \mathbf{H_{eff}} - \frac{\alpha\gamma}{\mathbf{M_s}}[\mathbf{M} \times \mathbf{M} \times \mathbf{H_{eff}}] \tag{6.1}$$

Here, $\mathbf{M_s}$ is the saturation magnetization of the material, γ is the gyro-magnetic ratio, and α is a damping constant. The effective magnetic field ($\mathbf{H_{eff}}$) is the average magnetic field experienced by the magnetic moment, and it is the sum of externally applied field ($\mathbf{H}$), the dipole field and the uniaxial anisotropy field

$$\mathbf{H_{eff}^i} = \mathbf{H} - \mathbf{H_{dp}^i} + 2K\frac{\mathbf{M.u}}{\mathbf{M_s^2}}\mathbf{u} \tag{6.2}$$

where $\mathbf{u}$ is a unit vector in the direction of the magneto-crystalline anisotropy and K is the strength of the anisotropy. The dipole field on the i-th nanomagnet is given by

$$\mathbf{H_{dp}^i} = \sum_{j \neq i}[\frac{\mathbf{M_j}}{\mathbf{r_{ij}^3}} - 3\frac{(\mathbf{M_j.r_{ij}})}{\mathbf{r_{ij}^5}}] \tag{6.3}$$

The software approximates the continuum micromagnetic theory, where continuous magnetization distribution of a magnetic material is approximated by a discrete magnetization distribution consisting of equal volume cubes (3-D). The software approximates the continuum micromagnetic theory, where continuous magnetization distribution of a magnetic material is approximated by a discrete magnetization distribution consisting of equal volume cubes (3-D). The cubic cell size in all the simulations were kept 5nm, which is smaller than the characteristic exchange length of permalloy, $l_{ex} = [2A_{ex}/(\mu_0 M_s^2)]^{1/2} \approx 5.2$ nm.

Table 6.1 Magnetic properties of permalloy material used in simulation study.

Material parameters used in simulation	
Saturation Magnetization (M_s)	800
Exchange stiffness constant (A)	$1.3 X 10^{-12}$
Anisotropy Constant (K)	1.05
Damping constant (α)	0.5

Within each cell, the magnetization is assumed to be uniform and is represented by a three dimensional spin vector M. In this study, we have studied the equilibrium magnetization configuration of the nanomagnet, which results from the minimization of the free energy. The energy of magnetic structure is composed of 1) the exchange energy E_{ex} between nearest neighbors which is characterized by the exchange coupling constant A (erg/cm); 2) the magnetocrystalline anisotropy energy E_K. It describes the interaction of magnetic moments with the crystal, which is characterized by the constant K; 3) the demagnetization energy E_D, which results from the interaction of the magnetic moments due to the volume or surface magnetic charge distribution associated to the magnetization distribution inside a magnet; 4) zeeman energy E_z, which arises from the interaction of magnetic moments with an externally applied field and causes rotation of magnetization in the magnetic structure. In this frame of work permalloy material is used with magnetic properties as shown in Table 6.1.

6.3 Results and Discussion

The nanoscale structure behaves differently than the bulk material. In the nanoscale magnet the interaction between competent magnetostatic energy and quantum mechanical exchange energy, cause the nanomagnet to behave as single spin [56]. There are two possible
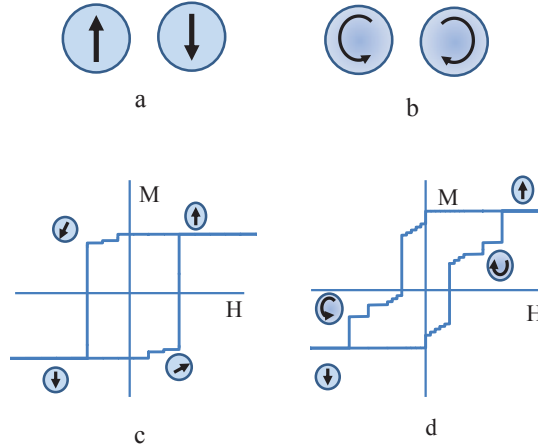
Figure 6.3 Two possible stable state of nanomagnet (a) magnetization configuration in single domain state, (b) magnetization configuration of vortex state, (c) coherent magnetization reversal in single domain state and (d) curly magnetization reversal in vortex state.

stable states in single domain nanomagnet. One is the Single domain state where all the moment align in one direction either up or down at ground state, which may represent as Boolean logic 1 or 0 as shown in Figure6.3(a) and the reversal of magnetization is coherent as shown in Figure 6.3(c). Second is the vortex state, first demonstrated by Shinjo et.al. [91], where moments have the curling spin configuration, has the low energy configuration and magnetization can be clock-wise or counter clock wise as shown in Figure6.3(b) and the reversal takes by formation of nucleation and annihilation under the applied field as shown in Figure fig1 d. The micromagnetic numerical simulation study plays an essential role in understanding and designing nanoscale element. Prior to the whole system implementation (e.g computation array), it is important to understand well fundamental properties of individual and interacting nanomagnet elements with reduced dimensions. In this work we have been used the circular shaped dots, as previous literature reviewed a great attention towards this shape.
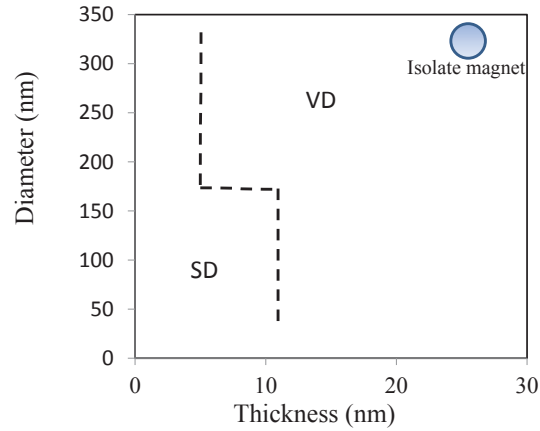
Figure 6.4 A phase diagram of numerical simulation results for isolate nanomagnet, as a function of element size and thickness the finally attained magnetization state. The solid line shows the boundary demarcate the single domain state and vortex state.

6.3.1 Isolated Nanomagnet

Generally for given material, the geometry determines which kind of magnetization configuration may be present, while the size and lateral dimension control the balance between the demagnetization field and exchange field, which in turn determine the transformation of one magnetization configuration into another Therefore, in order to estimate the critical properties (switching field (corecivity), magnetization reversal process etc.), single or isolate nanomagnet study is ideal case.

The first study in this work involve the determination of boundary between single domain and vortex state of isolated circular nanomagnet. We have simulated the permalloy circular nanomagnet with diameter 100-300nm and thickness 5-20nm. For each simulation, a uniformly magnetized state in X-axis, 10way from the ground state direction was used as the initial condition. Our results matches with the previous studies [92], suggested that the diameter and thickness of the dots determines whether the nanomagnet is single domain or vortex state. Based on result we have produced the phase diagram as shown in Figure 6.4,
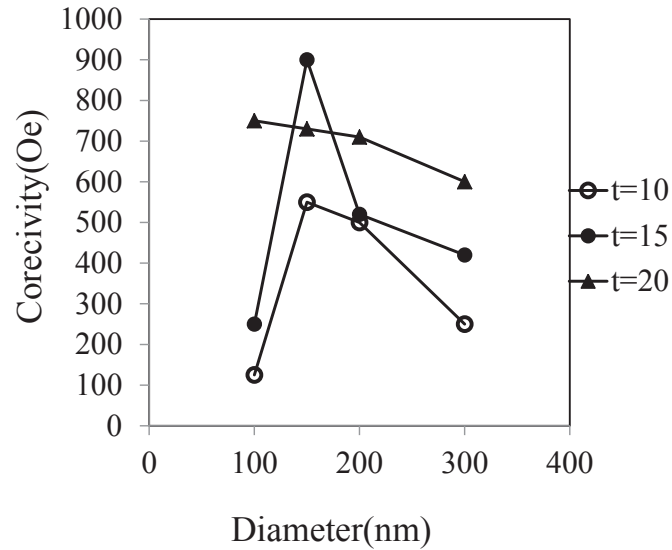
Figure 6.5 Corecivity of isolated nanomagnet for different diameters with respect to thickness.

demarcating the two states. The result shows that the vortex state is present in the thick nanomagnet while thinner nanomagnet show single domain state.

Another important property that is greatly influence by nanomagnet dimension is the corecivity or switching field, which is the field required to reverse the state of nanomagnet. Figure 6.5 summarize the data for the variation of the switching field (corecivity) from single domain state and vortex state for an isolate nanomagnet as a function of thickness. This reveals that as long as nanomagnet is in single domain state, the corecivity increases with thickness as shown in Figure 6.5, the nanomagnet with thickness 15nm has high corecivity then thickness 10nm for nanomagnet with diameter 100nm and 150nm, have single domain state. Another important observation is that the corecivity decreases, when nanomagnet transit from single domain state to vortex state, as shown in Figgure 6.5 the nanomagnet with diameter 200nm and 300nm with thickness 10nm and 15nm are in vortex state , has less corecivity than nanomagnet with same thickness but with diameter less than 200nm. Furthermore the nanomagnet with thickness 20nm has vortex state irrespective of the di-
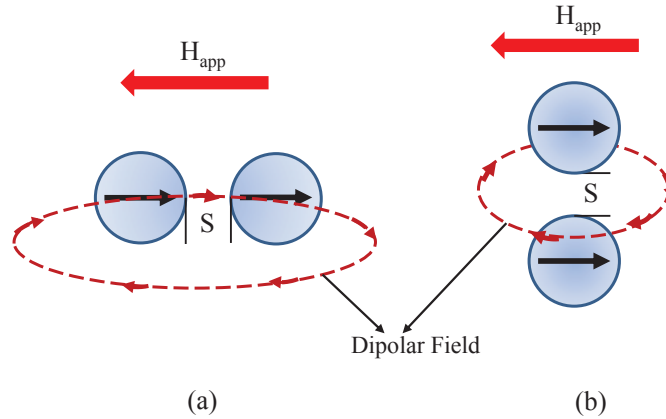
Figure 6.6 Coupling arrangements (a) Longitudinal arrangement and (b) Transverse arrangement.

ameter as shown in Figure 6.4, the corecivity decreases with the increase of diameter as shown in Figure 6.5.

6.3.2 Coupled Nanomagnet

The study described in the previous section is now extended to the case of coupled nanomagnet. Due to the $1/r^3$ dependence of the dipole-dipole interaction, the effect of the interaction between nanomagnets depends strongly on the distance between the neighboring nanomagnet.

In order to capture, to first order, the effect of the dipolar interaction on the magnetization state, we first examine the two single domain nanomagnet with (a) longitudinal arrangement, where magnetic moments are parallel to each other and also to their separation and (b) transverse arrangement, where magnetic moments are parallel to each other but perpendicular to their separation.

In longitudinal arrangement, the dipolar interaction between two nanomagnets is parallel and anti-parallel to the direction of applied field as shown in Figure 6.6(a), While in trans-
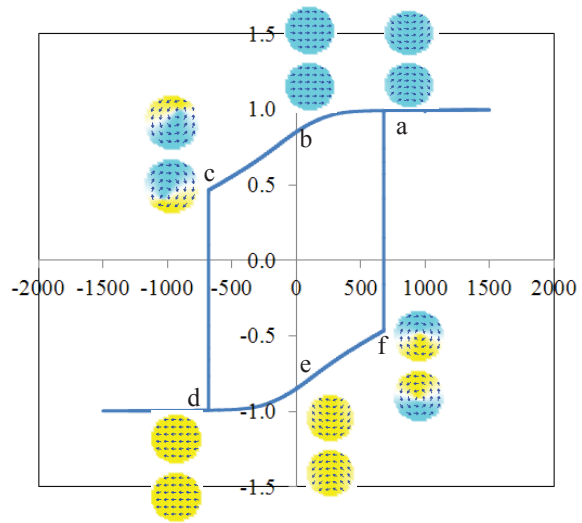
Figure 6.7 Magnetization transition process in Transverse arrangement.
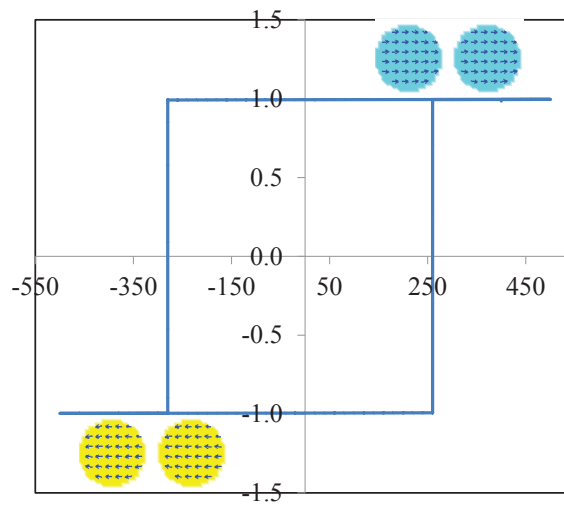
Figure 6.8 Magnetization transition process in Longitudinal arrangement.
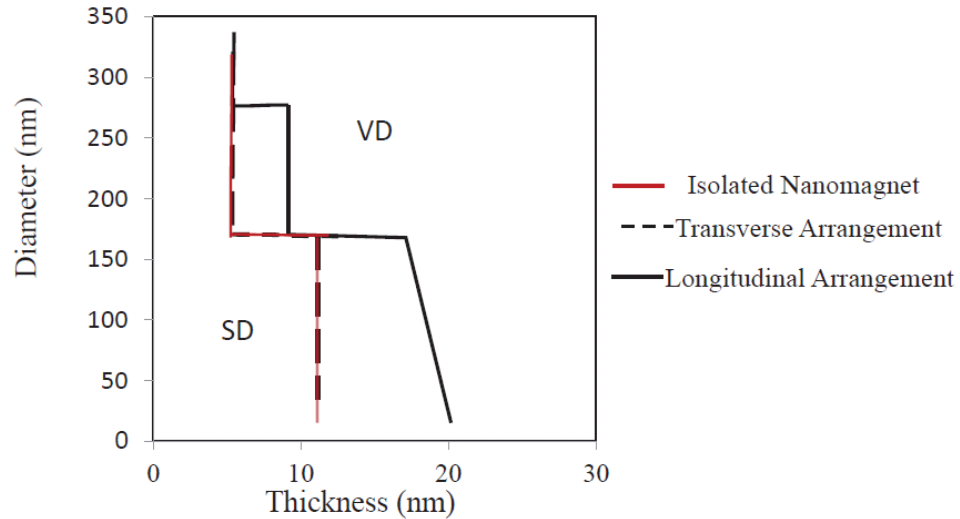
Figure 6.9 A phase diagram of numerical simulation results for isolated and coupled nano-magnet, as a function of element size and thickness. The solid red line shows the boundary between the single domain state (SD) and vortex state (VD) for isolated nanomagnet. The solid black line is the boundary for longitudinal arrangement, while dashed black line is the boundary for the transverse arrangement.

verse arrangement, the dipolar interaction between two nanomagnet is anit-parallel and it is parallel to the applied field as shown in the Figure 6.6(b). In order to elaborate the dipolar interaction on the magnetization transition state, a simulation was carried out for both arrangement with 100nm diameter nanomagnet. The simulation results shows a clear difference in the magnetization transition for longitudinal and transverse arrangement. The nanomagnet with longitudinal arrangement with spacing 20nm has gone through the coher-ent reversal with one step switching as shown in Figure 6.7, while in transverse arrangement of nanomagnet the reversal takes place gradually through the vortex formation.

The simulation experiment is repeated for different diameters and thicknesses. The re-sults are represented in the form of phase diagram. It is evident that nanomagnets with 20 *nm* thickness and 100 *nm* diameter in longitudinal arrangement stays in single domain state during switching, which is not the case when nanomagnets of same dimension is iso-

Figure 6.10 Simulated hysteresis loop for 3 x 3 array of 100 *nm* diameter with different thickness indicated above the loop.

lated or in transverse arrangement, as shown in Figure 6.9. So, in general the phase plot of longitudinally coupled nanomagnet moves upward as compared to the transverse and single nanomagnet. It is noteworthy that the dipolar interaction between two single domain nanomagnets that is sufficient to produce collective rotation of magnetic spin during magnetization reversal, depends on their thickness and diameter.

Apart from the dimension and inter-element distance, another important factor that influences the dipolar interaction is the number of nearest nanomagnets in an array. In order to visualize the effect of dipole-dipole interaction in 2D array, we carried out simulation for different size arrays (3 x 3 and 5 x 5). The diameter and inter-element separation is kept constant at 100 *nm* and 20 *nm* respectively, while thickness is varied between $5 - 20$ *nm*.

The saturation field of 100 *mT* along the array edge is applied. The magnetic moments of nanomagnet rotates in order to minimize the magneto-static energies due to uncompen-
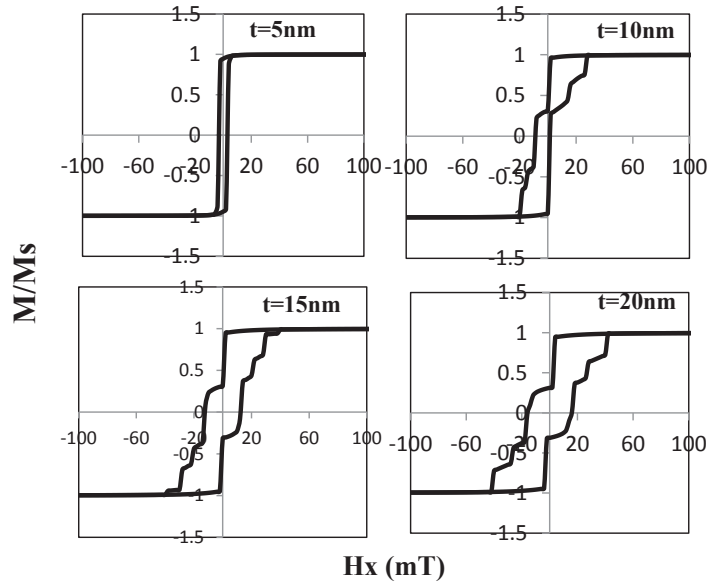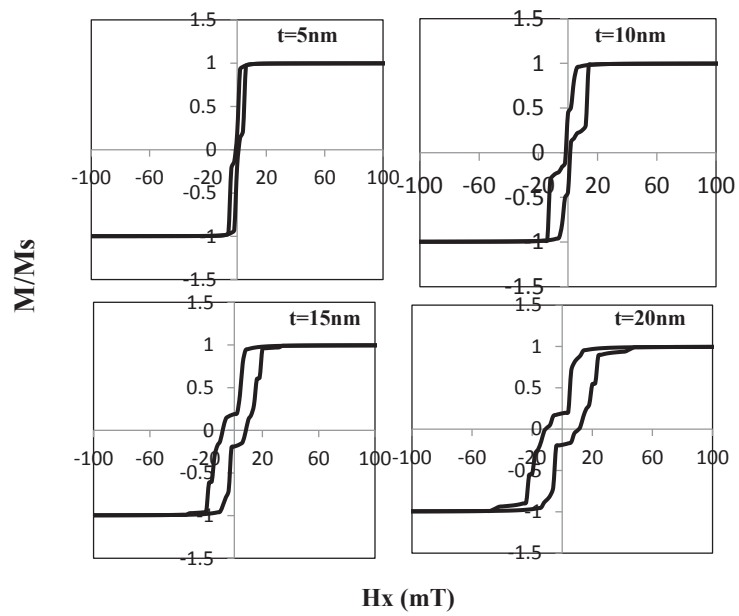
Figure 6.11 Simulated hysteresis loop for 5 x 5 array of 100 *nm* diameter with different thickness indicated above the loop.
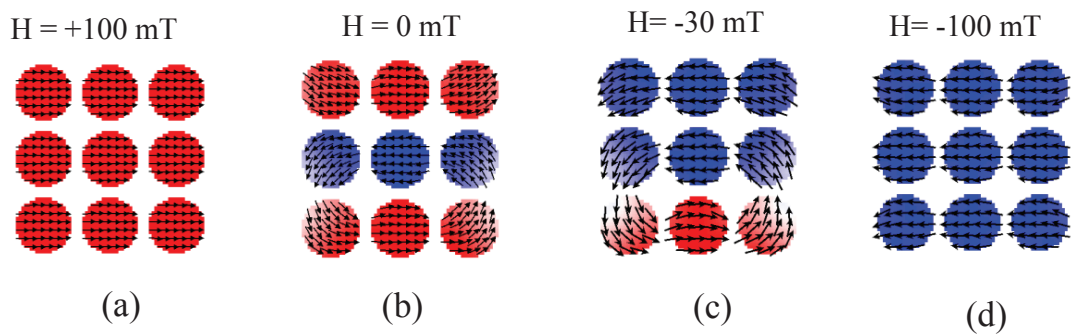
Figure 6.12 Spin configuration of 3 x 3 array at different field, during reversal process.
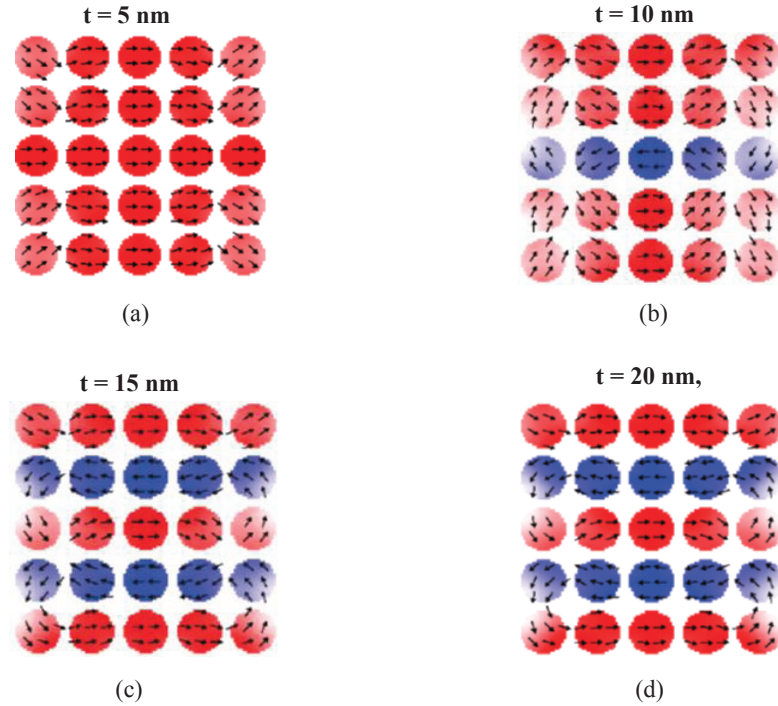
Figure 6.13 Spin configuration of 5 x 5 array at remenance with different thickness.

sated nanomagnets. A change in remanent magnetization and the area A_h enclosed by the hysteresis loop, with respect to thickness during reversal process is observed as shown in Figure 6.10 and Figure 6.11. It is evident from the magnetization curve that due to dipolar interaction, the reversal tends to occur by jumps rather than by reversible rotations. Also reversal in an array takes place hierarchically, starting with the inner most row and proceeding to the outer row as shown in Figure 6.12.

The dipolar interaction between the nanomagnets is increased with increase in thickness of nanomagnets as substantiated by simulation results. Illustrated in Figure 6.13 is the equilibrium spin configuration for 5 x 5 array with different thickness. Clearly, magnetization for array with thickness 5 *nm* and 10 *nm* are not aligned in anti-ferromagnetic order as shown in Figure 6.13 (a) and (b). This configuration indicates that nanomagnets in the array are weakly coupled as opposed to the array of nanomagnets with thickness 15 *nm* and 20 *nm*,
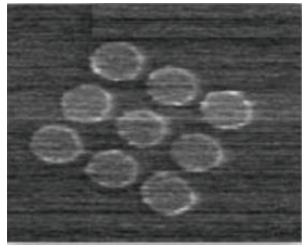
(a)
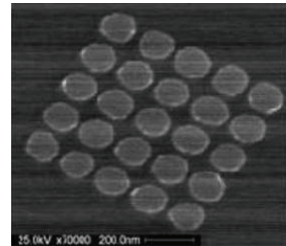
(d)
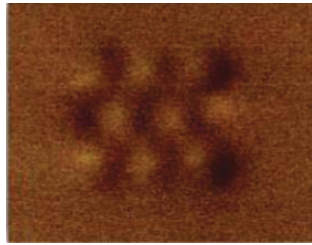
(b)
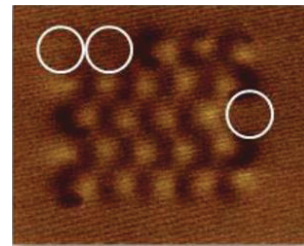
(e)
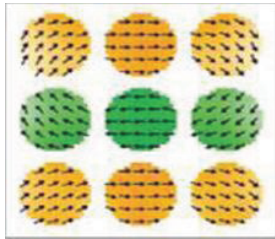
(c)
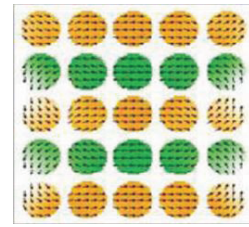
(f)

Figure 6.14 (a) SEM image of 3 x 3 array, (b) MFM image of 3 x 3 array, at remenance (c) Simulated spin configuration, (d) SEM image for 5 x 5 array, (e) MFM image of 5 x 5 array, at remenance. MFM tip couldn't capture the image of the nanomagnets showed by white circles due to very low magnetization of the nanomagnet because of the rough surface of the nanomagnet and (f) Simulated spin configuration.

where nanomagnets are strongly coupled and attain the anti-ferromagnetic order as shown in Figure 6.13 (c) and (d).

We have fabricated arrays of 100 *nm* diameter circular nanomagnet with thickness 15 *nm* to validate some of the findings. We were able to achieve edge to edge spacing of 20 *nm* by E-beam lithography and this indicates that it is possible to fabricate nanosize magnet with such a small separation. Figure 6.14(a) and (c), shows the MFM images of 3 x 3 and 5 x 5 array, at remanence, after saturating the array and reducing the field back to zero. The images reveals the antiferromagnetic ordering, which are the consequences of the strong dipole-dipole interaction between the nanomagnets. These results are correlated with the numerical simulation as shown in Figure 6.14(b) and (d).

6.4   Conclusion

We have studied the magnetization state transition in coupled nanomagnets, for two basic configurations namely, longitudinal and transverse. The phase diagram between vortex state and single domain state was produced for both the configurations. We find that single domain state in longitudinal arrangement is present over a large range of thickness as compared to the transverse and isolated nanomagnet. This is useful to know when we design computing system where switching through a single state is desirable. Further, we studied theoretically and experimentally the magnetization state of the finite arrays. The study predicted that the array of diameter 100 *nm* and thickness $15-20$ *nm*, stays in single domain state with one step reversal, which results in fast switching and is ideal for computation applications.

CHAPTER 7

CONCLUSION

7.1   Summary

This research work is a blend of two fields: micro-magnetic and applied device design, where the novel field coupled computing paradigm known as magnetic cellular automata is investigated. Todays silicon transistor based technology, which relies on the electric current and voltage for information processing, will reach the limits of miniaturization and power efficiency [1]. This work focused on a different approach in which the spin of electron is exploited and manipulated, hence the processing is entirely magnetic in nature. One of the promising architecture for such processing is field coupled computing, where individual element switched under the influence of mutual interaction of neighboring element. The magnetic computing shows the promising technology for the near future as the same element can store and process data that could lead to programmable logic. Currently, our group is extensively involved in verifying magnetic structure experimentally and theoretically.

We have reviewed the fundamental limits the current technology will face in coming decade. Besides, the emerging alternative technique to CMOS is explored. The magnetic cellular automata (MCA) has prospects as future technology due to numerous advantages such as room temperature operation, high density, low power dissipation and non-volatile operation. For past ten years, significant amount of research has been performed on MCA architecture, which includes the successful experimental demonstration of working boolean

logic gates, fan-out circuit and cross-over wire architecture. The fundamental problem with magnetic cellular automata architecture is the directional flow of information from input to output with out magnetic frustration. In this work, we made the effort to resolve this problem by proposing an novel spatially moving Landauer clock that assures correct operation irrespective of the array length. The MCA operation under Landauer clock, utilizes interaction of three fields: Null field, Switch field and Input field. In this clocking scheme the Null field is removed from nanomagnet one at a time as compared to the conventional clock [6], where magnetic field is removed from a group of nanomagnet. Further, the study is extended to investigate the effect of clock field strength on different nanomagnet shapes with varying aspect ratio. It was concluded that oval shaped nanomagnet require more clock field as compared to the rectangular shaped nanomagnet. All the results presented in this work is generated by OOMMF package, which is best open source code with the ability to reproduce experimental results.

In order to harvest the essence of nanoscale magnetic element for computation, reliability study of nanoscale element is indispensable. In this framework, we have done an extensive defect analysis of MCA array. The study focused on fabrication variation defect under spatially moving clock. The prime stress on six type of defects: irregular spacing, missing material, bulging, missing cell, partial merge cell and fully merge cell. The irregular spacing defect and missing material defect, which are usually encountered during the fabrication process does not affect the correct flow of operation, hence constitutes the robust architecture. We have also performed study with respect to location of the defect in different length array and showed that location and array length has no affect on defect masking. Another important aspect investigated in this dissertation is the study of dipolar interaction between elements of 2D nanomagnet array. The study reveals that nanomagnet having single domain state has fast switching operation and strong dipolar interaction, which is

ideal for the computation application. The results show that nanomagnet with diameter 100 *nm* and thickness 15 *nm* is ideal for the computation application.

Currently, extensive research on this technology is progressing at an institutional level and most likely commercial companies will take over the research. However, it is expected to hit the market in the near future. Conversely, there is no definite answer whether or not this will replace the existing CMOS technology, but since MRAM is already established and shown such a wide impact in the market. Therefore, this appears promising that we will see the Magnetic Field Coupled (MFC) based architecture.

7.2   Future Work

We have explored and discussed the novel device based on the magnetic field interaction, which is realized by ferromagnetic elongated element having characteristic of shape anisotropy. There are numerous opportunities for research on magnetic cellular auotmata including the investigations presented in this dissertation. One area requiring substantial additional research clearly lies in the experimental implementation of the clocking system for MCA architecture. Further more , it is required to investigate the method to localize the magnetic field in nanoscale size magnets for developing a fully functional MCA system. Our group is trying to use MFM tip stray field to manipulate and control the magnetic state of individual element of magnetic logic.

The defect study presented in chapter 5 can be extended from single defect to multiple defect in an array and further extensive defect analysis can be studied. Surface roughness can be modeled to study the effectiveness of the surface roughness on the correct flow of information, which is not included in the current work. The finite 2D nanomagnet array study presented in chapter 6 provides basis for the future research in the programmable logic computation.

In order to optimize the nanomagnet device for high speed, reduced power, and the clock field, alternative material needs to be investigated. Additionally, the magnetic device can be further optimized for high speed and low clock field by utilizing the multi-layer structure. Future work also requires to devise an efficient quantum model that will help to study the accurate dynamic evolution of the system, which is essential to estimate the reliability and operational frequency.

REFERENCES

[1] "International technology roadmap for semiconductor," 2002.

[2] P. W., C. G., and C. A., "Field-coupled devices for nanoelectronic integrated circuits," *Nanotechnology, 2001. IEEE-NANO 2001. Proceedings of the 2001 1st IEEE Conference on*, pp. 313–318, 2001.

[3] C. S. Lent, P. D. Tougaw, W. Porod, and G. H. Bernstein, "Quantum cellular automata," *Nanotechnology*, vol. 4, pp. 49–57, jan 1993.

[4] W. A. Goddard, D. W. Brenner, and S. E. Lyshevski, *Handbook of Nanoscience, Engineering, and Technology*, 2003.

[5] J. F. Pulecio and S. Bhanja, "Magnetic cellular automata coplanar cross wire systems," *Journal of Applied Physics*, vol. 107, no. 3, pp. 034 308 –034 308–5, feb 2010.

[6] M. Alam, M. Niemier, W. Porod, S. Hu, M. Putney, and J. DeAngelis, "On-chip clocking scheme for nanomagnet qca," *Device Research Conference, 2007 65th Annual*, pp. 133–134, June 2007.

[7] Y. B. Taur, D. A. Chen, W. Frank, D. J. Ismail, K. E. Lo, S.-H. Sai-Halasz, G. A. Viswanathan, R. G. Warm, and H.-J. C. Wind, "CMOS Scaling into the Nanometer Regime," *PROCEEDINGS- IEEE*, vol. 85, no. 4, pp. 486–504, 1997.

[8] H.-S. P. F. Wong, D. J. Solomon, P. M. Warm, C. H. J. Welser, and J. J., "Nanoscale CMOS," *PROCEEDINGS- IEEE*, vol. 87, no. 4, pp. 537–570, 1999.

[9] P. PEERCY, "The drive to miniaturization : The future of microelectronics," *Nature*, vol. 406, no. 11, pp. 1023–1026, 2000.

[10] R. Eisberg and R. Resnick, *Quantum Physics of Atoms, Molecules, Solids, Nuclei, and Particles, 2nd Edition*, Eisberg, R. & Resnick, R., Ed., Jan. 1985.

[11] Y. Asai, S. Wada, "Technology challenges for integration near and below 0.1 um," *IEEE INSTITUTE OF ELECTRICAL AND ELECTRONICS*, vol. 85, no. 4, pp. 505–520, 1997.

[12] R. Compano, L. Molenkamp, and D. Paul, "Technology Roadmap for Nano-electronics. 1999. Produced under the European Commissions Microelectronics Advanced Research Initiative (MELARI). Internet address." [Online]. Available: http://www.cordis.lu/esprit/src/melari.htm.

[13] D. Clark, "Teramac: Pointing the way to real-world nanotechnology," *Computing in Science and Engineering*, vol. 5, pp. 88–90, 1998.

[14] J. Hergenrother, D. Monroe, F. Klemens, A. Komblit, G. Weber, W. Mansfield, M. Baker, F. Baumann, K. Bolan, J. Bower, N. Ciampa, R. Cirelli, J. Colonell, D. Eaglesham, J. Frackoviak, H. Gossmann, M. Green, S. Hillenius, C. King, R. Kleiman, W. Lai, J.-C. Lee, R. Liu, H. Maynard, M. Morris, S.-H. Oh, C.-S. Pai, C. Rafferty, J. Rosamilia, T. Sorsch, and H.-H. Vuong, "The vertical replacement-gate (vrg) mosfet: a 50-nm vertical mosfet with lithography-independent gate length," in *Electron Devices Meeting, 1999. IEDM Technical Digest. International*, 1999.

[15] D. Hisamoto, W.-C. Lee, J. Kedzierski, H. Takeuchi, K. Asano, C. Kuo, E. Anderson, T.-J. King, J. Bokor, and C. Hu, "Finfet-a self-aligned double-gate mosfet scalable to 20 nm," *Electron Devices, IEEE Transactions on*, vol. 47, no. 12, pp. 2320 – 2325, Dec. 2000.

[16] S. Harrison, P. Coronel, F. Leverd, R. Cerutti, R. Palla, D. Delille, S. Borel, S. Jullian, R. Pantel, S. Descombes, D. Dutartre, Y. Morand, M. Samson, D. Lenoble, A. Talbot, A. Villaret, S. Monfray, P. Mazoyer, J. Bustos, H. Brut, A. Cros, D. Munteanu, J.-L. Autran, and T. Skotnicki, "Highly performant double gate mosfet realized with son process," in *Electron Devices Meeting, 2003. IEDM '03 Technical Digest. IEEE International*, 2003, pp. 18.6.1 – 18.6.4.

[17] J. Deng, A. Lin, G. C. Wan, and H.-S. P. Wong, "Carbon nanotube transistor compact model for circuit design and performance optimization," *J. Emerg. Technol. Comput. Syst.*, vol. 4, no. 2, pp. 1–20, 2008.

[18] P. N. T. D. C. Bachtold, A. Hadley, "Logic circuits with carbon nanotube transistors," *SCIENCE -NEW YORK THEN WASHINGTON*, pp. 1317–1319, 2001.

[19] K. Natori, Y. Kimura, and T. Shimizu, "Characteristics of a carbon nanotube field-effect transistor analyzed as a ballistic nanowire field-effect transistor," *Journal of Applied Physics*, vol. 97, no. 3, pp. 034 306–+, feb 2005.

[20] A. Raychowdhury, S. Mukhopadhyay, and K. Roy, "A circuit-compatible model of ballistic carbon nanotube field-effect transistors," *Computer-Aided Design of Integrated Circuits and Systems, IEEE Transactions on*, vol. 23, no. 10, pp. 1411–1420, Oct. 2004.

[21] B. C. Paul, S. Fujita, M. Okajima, and T. Lee, "Modeling and analysis of circuit performance of ballistic cnfet," in *DAC '06: Proceedings of the 43rd annual conference on Design automation*. New York, NY, USA: ACM, 2006, pp. 717–722.

[22] D. D. D. Ma, C. S. Lee, F. C. K. Au, S. Y. Tong, and S. T. Lee, "Small-Diameter Silicon Nanowire Surfaces," *Science*, vol. 299, no. 5614, pp. 1874–1877, 2003. [Online]. Available: http://www.sciencemag.org/content/299/5614/1874.abstract

[23] K. Buddharaju, N. Singh, S. Rustagi, S. Teo, L. Wong, L. Tang, C. Tung, G. Lo, N. Balasubramanian, and D. Kwong, "Gate-all-around si-nanowire cmos inverter logic fabricated using top-down approach," in *Solid State Device Research Conference, 2007. ESSDERC 2007. 37th European*, 2007, pp. 303 –306.

[24] M. A. Kastner, "The single-electron transistor," *Rev. Mod. Phys.*, vol. 64, no. 3, pp. 849–858, Jul 1992.

[25] H. Inokawa, A. Fujiwara, and Y. Takahashi, "A multiple-valued logic and memory with combined single-electron and metal-oxide-semiconductor transistors," *Electron Devices, IEEE Transactions on*, vol. 50, no. 2, pp. 462 – 470, 2003.

[26] C. K. Lee, S. J. Kim, S. J. Shin, J. B. Choi, and Y. Takahashi, "Single-electron-based flexible multivalued logic gates," *Applied Physics Letters*, vol. 92, no. 9, pp. 093 101 –093 101–3, Mar. 2008.

[27] K. Song, Y. K. Lee, J. S. Sim, H. Jeoung, J. D. Lee, B. Park, Y. S. Jin, and Y. W. Kim, "SET/CMOS Hybrid Process and Multiband Filtering Circuits," *IEEE Transactions on Electron Devices*, vol. 52, pp. 1845–1850, Aug. 2005.

[28] M. Saitoh, H. Harata, and T. Hiramoto, "Room-Temperature Demonstration of Integrated Silicon Single-Electron Transistor Circuits for Current Switching and Analog Pattern Matching," *IEDM Tech. Dig*, 2004.

[29] P. Xu, K. Xia, C. Gu, L. Tang, H. Yang, and J. Li, "An all-metallic logic gate based on current-driven domain wall motion," 2008.

[30] M. Hayashi, L. Thomas, R. Moriya, C. Rettner, and S. S. P. Parkin, "Current-Controlled Magnetic Domain-Wall Nanowire Shift Register," *Science*, vol. 320, no. 5873, pp. 209–211, 2008. [Online]. Available: http://www.sciencemag.org/content/320/5873/209.abstract

[31] J. Yoon, J.-C. Lee, C.-Y. You, S.-B. Choe, K.-H. Shin, and M.-H. Jung, "Current- and field-driven domain wall motion in l- and c-shaped permalloy nanowires with different wire widths," *Magnetics, IEEE Transactions on*, vol. 44, no. 11, pp. 2527 –2530, 2008.

[32] R. Kummamuru, A. Orlov, R. Ramasubramaniam, C. Lent, G. Bernstein, and G. Snider, "Operation of a quantum-dot cellular automata (qca) shift register and analysis of errors," *IEEE Transactions on Apllied Physics*, vol. 50, no. 9, pp. 1906–1913, September 2003.

[33] A. Orlov, R. Kummamuru, R. Ramasubramaniam, C. Lent, G. Bernstein, and G. Snider, "Clocked quantum-dot cellular automata shift register," *Surface Science*, vol. 532, pp. 1193–1198, 2003.

[34] ——, "A two-stage shift register for clocked quantum-dot cellular automata," *Journal of Nanoscience and Nanotechnology*, vol. 2, pp. 351–355, 2002.

[35] I. Amlani, A. Orlov, G. Snider, C. Lent, W. Porod, and G. Bernstein, "Digital logic gate using quantum-dot cellular automata," *Science*, vol. 284, pp. 289–291, April 1999.

[36] G. Snider, A. Orlov, I. Amlani, G. Bernstein, C. Lent, J. Merz, and W. Porod, "Quantum-dot cellular automata: Line and majority logic gate," *Japanese Journal of Applied Physics*, vol. 38, no. 12B, pp. 7227–7229, Dec 1999.

[37] V. Vankamamidi, M. Ottavi, and F. Lombardi, "A line-based parallel memory for QCA implementation," *IEEE Transactions on Nanotechnology*, vol. 4, no. 6, pp. 690 – 698, Nov. 2005.

[38] A. Aviram, "Molecules for memory, logic, and amplification," *Journal of the American Chemical Society*, vol. 110, no. 17, pp. 5687–5692, 1988. [Online]. Available: http://pubs.acs.org/doi/abs/10.1021/ja00225a017

[39] N. S. Hush, A. T. Wong, G. B. Bacskay, and J. R. Reimers, "Electron and energy transfer through bridged systems. 6. molecular switches: the critical field in electric field activated bistable molecules," *Journal of the American Chemical Society*, vol. 112, no. 11, pp. 4192–4197, 1990. [Online]. Available: http://pubs.acs.org/doi/abs/10.1021/ja00167a014

[40] C. S. Lent, B. Isaksen, and M. Lieberman, "Molecular quantum-dot cellular automata," *Journal of the American Chemical Society*, vol. 125, no. 4, pp. 1056–1063, 2003. [Online]. Available: http://pubs.acs.org/doi/abs/10.1021/ja026856g

[41] R. P. Cowburn, D. K. Koltsov, A. O. Adeyeye, and M. E. Welland, "Probing submicron nanomagnets by magneto-optics," *Applied Physics Letters*, vol. 73, pp. 3947–+, dec 1998.

[42] R. P. Cowburn, D. K. Koltsov, A. O. Adeyeye, M. E. Welland, and D. M. Tricker, "Single-domain circular nanomagnets," *Phys. Rev. Lett.*, vol. 83, no. 5, pp. 1042–1045, Aug 1999.

[43] G. Csaba, "Computing with filed-coupled nanaomagnets," Ph.D. dissertation, University of Notre Dame, 2003.

[44] G. Csaba and W. Porod, "Simulation of field coupled computing architectures based on magnetic dot arrays," *Journal of Computational Electronics*, vol. 1, no. 1, pp. 87–91, july 2002.

[45] C. G. P. W. L. P. and C. A. I, "Activity in field-coupled nanomagnet arrays," *INTERNATIONAL JOURNAL OF CIRCUIT THEORY AND APPLICATIONS*, vol. 35, no. 3, pp. 281–293, 2007.

[46] C. G., L. P., and P. W., "Power dissipation in nanomagnetic logic devices," *Nanotechnology, 2004. 4th IEEE Conference on*, pp. 346–348, Aug. 2004.

[47] D. A. Allwood, G. Xiong, M. D. Cooke, C. C. Faulkner, D. Atkinson, N. Vernier, and R. P. Cowburn, "Submicrometer ferromagnetic not gate and shift register," *Science*, vol. 296, pp. 2003–2006, june 2002.

[48] A. Imre, G. Csaba, L. Ji, A. Orlov, G. H. Bernstein, and W. Porod, "Majority Logic Gate for Magnetic Quantum-Dot Cellular Automata," *Science*, vol. 311, pp. 205–208, jan 2006.

[49] S. A. Haque, M. Yamamoto, R. Nakatani, and Y. Endo, "Magnetic logic gate for binary computing," *Science and Technology of Advanced Materials*, vol. 5, no. 1-2, pp. 79 – 82, 2004, 21st Century COE Program, Osaka University. [Online]. Available: http://www.sciencedirect.com/science/article/B6W6M-4BM684C-8/2/ebd7a704124abb34aca7dd22df6fc4f7

[50] E. Varga, S. Liu, M. Niemier, W. Porod, X. Hu, G. Bernstein, and A. Orlov, "Experimental demonstration of fanout for nanomagnet logic," in *Device Research Conference (DRC), 2010*, 2010, pp. 95 –96.

[51] M. Niemier, M. Alam, X. S. Hu, G. Bernstein, W. Porod, M. Putney, and J. DeAngelis, "Clocking structures and power analysis for nanomagnet-based logic devices," in *ISLPED '07: Proceedings of the 2007 international symposium on Low power electronics and design*.   New York, NY, USA: ACM, 2007, pp. 26–31.

[52] A. Kumari, J. F. Pulecio, and S. Bhanja, "Defect characterization in magnetic field coupled arrays," in *Proceedings of the 2009 10th International Symposium on Quality of Electronic Design*.   Washington, DC, USA: IEEE Computer Society, 2009, pp. 436–441. [Online]. Available: http://portal.acm.org/citation.cfm?id=1547561.1548399

[53] A. Kumari and S. Bhanja, "Landauer clocking for magnetic cellular automata (mca) arrays," *Very Large Scale Integration (VLSI) Systems, IEEE Transactions on*, 2010.

[54] S. Chikazumi, *Physics of Ferromagnetism*, Chikazumi,S., Ed., 1997.

[55] A. Aharoni, *Introduction to the theory of ferromagnetism*, Aharoni, A., Ed., 2000.

[56] W. Brown, *Micromagnetics*, Wiley, New York, Ed., 1963.

[57] N. Dao, S. R. Homer, and S. L. Whittenburg, "Micromagnetics simulation of nanoshaped iron elements: Comparison with experiment," *Journal of Applied Physics*, vol. 86, no. 6, pp. 3262–3264, 1999. [Online]. Available: http://link.aip.org/link/?JAP/86/3262/1

[58] N. Dao, S. L. Whittenburg, Y. Hao, C. A. Ross, L. M. Malkinski, and J. Q. Wang, "Magnetization reversal of elliptical co/cu/co pseudo-spin valve dots," *Journal of Applied Physics*, vol. 91, no. 10, pp. 8293 –8295, May 2002.

[59] M. Natali, A. Lebib, Y. Chen, I. L. Prejbeanu, and K. Ounadjela, "Configurational anisotropy in square lattices of interacting cobalt dots," *Journal of Applied Physics*, vol. 91, no. 10, pp. 7041–7043, 2002. [Online]. Available: http://link.aip.org/link/?JAP/91/7041/1

[60] R. Engel-Herbert, S. A. Haque, and T. Hesjedal, "Systematic investigation of Permalloy nanostructures for magnetologic applications," *Journal of Applied Physics*, vol. 101, no. 9, pp. 090 000–+, May 2007.

[61] A. Imre, G. Csaba, G. H. Bernstein, W. Porod, and V. Metlushko, "Investigation of shape-dependent switching of coupled nanomagnets," *Superlattices and Microstructures*, vol. 34, pp. 513–518, sep 2003.

[62] J. M. Deutsch, T. Mai, and O. Narayan, "Hysteresis multicycles in nanomagnet arrays," *Phys. Rev. E*, vol. 71, no. 2, p. 026120, Feb 2005.

[63] M. Niemier, A. Dingler, and X. Hu, "Design tradeoffs for improved performance in mqca-based systems," *Design and Test of Nano Devices, Circuits and Systems, 2008 IEEE International Workshop on*, pp. 35–38, Sept. 2008.

[64] C. Lent and B. Isaksen, "Clocked molecular quantum-dot cellular automata," *Electron Devices, IEEE Transactions on*, vol. 50, no. 9, pp. 1890–1896, Sept. 2003.

[65] C. S. Hennessy, K. Lent, "Clocking of molecular quantum-dot cellular automata," *Journal of Vacuum Science and Technology B Microelectronics and Nanometer structure*, vol. 19, no. 9, pp. 1752–1755, Sept. 2001.

[66] M. B. Tahoori, M. Momenzadeh, J. Huang, and F. Lombardi, "Defects and faults in quantum cellular automata at nano scale," in *VTS '04: Proceedings of the 22nd IEEE VLSI Test Symposium*. Washington, DC, USA: IEEE Computer Society, 2004, p. 291.

[67] M. Momenzadeh, J. Huang, and F. Lombardi, "Defect characterization and tolerance of qca sequential devices and circuits," in *DFT '05: Proceedings of the 20th IEEE International Symposium on Defect and Fault Tolerance in VLSI Systems*. Washington, DC, USA: IEEE Computer Society, 2005, pp. 199–207.

[68] M. Niemier, M. Crocker, and X. S. Hu, "Fabrication variations and defect tolerance for nanomagnet-based qca," in *DFT '08: Proceedings of the 2008 IEEE International Symposium on Defect and Fault Tolerance of VLSI Systems*. Washington, DC, USA: IEEE Computer Society, 2008, pp. 534–542.

[69] D. B. Carlton, N. C. Emley, E. Tuchfeld, and J. Bokor, "Simulation Studies of Nanomagnet-Based Logic Architecture," *Nano Letters*, vol. 8, pp. 4173–4178, Dec. 2008.

[70] "Nano-material, nano-manufacturing research center."

[71] J. Nabity, "nanometer pattern generation system."

[72] S. Y. Chou and Q. Xia, "Improved nanofabrication through guided transient liquefaction," *Nature Nanotechnology, Volume 3, Issue 6, pp. 369 (2008).*, vol. 3, pp. 369–+, june 2008.

[73] M. A. McCord and M. J. Rooks, *SPIE Handbook of Microlithography, Micromachining and Microfabrication*, 2003.

[74] M. J. Donahue, R. D. Mcmichael, R. D. McMichael, and R. B, "Exchange energy representations in computational micromagnetics," 1997.

[75] S. A. Wolf, D. D. Awschalom, R. A. Buhrman, J. M. Daughton, S. von Molnar, M. L. Roukes, A. Y. Chtchelkanova, and D. M. Treger, "Spintronics: A Spin-Based Electronics Vision for the Future," *Science*, vol. 294, no. 5546, pp. 1488–1495, 2001.

[76] S. Sarkar and S. Bhanja, "Direct quadratic minimization using magnetic field-based computing," in *NDCS '08: Proceedings of the 2008 IEEE International Workshop on Design and Test of Nano Devices, Circuits and Systems*. Washington, DC, USA: IEEE Computer Society, 2008, pp. 31–34.

[77] J. A. Johnson, M. Grimsditch, V. Metlushko, P. Vavassori, B. Ilic, P. Neuzil, and R. Kumar, "Magneto-optic Kerr effect investigation of cobalt and permalloy nanoscale dot arrays: Shape effects on magnetization reversal," *Applied Physics Letters*, vol. 77, pp. 4410–+, Dec. 2000.

[78] R. P. Cowburn and M. E. Welland, "Phase transitions in planar magnetic nanostructures," *Applied Physics Letters*, vol. 72, no. 16, pp. 2041 –2043, apr 1998.

[79] E. Seynaeve, G. Rens, A. V. Volodin, K. Temst, C. van Haesendonck, and Y. Bruynseraede, "Transition from a single-domain to a multidomain state in mesoscopic ferromagnetic Co structures," *Journal of Applied Physics*, vol. 89, pp. 531–534, Jan. 2001.

[80] M. Konoto, T. Yamada, K. Koike, H. Akoh, T. Arima, and Y. Tokura, "Formation and control of magnetic vortex chirality in patterned micromagnet arrays," *Journal of Applied Physics*, vol. 103, no. 2, pp. 023 904–+, Jan. 2008.

[81] J. F. Smyth, S. Schultz, D. Kern, H. Schmid, and D. Yee, "Hysteresis of submicron permalloy particulate arrays," *Journal of Applied Physics*, vol. 63, pp. 4237–4239, Apr. 1988.

[82] R. P. Cowburn, D. K. Koltsov, A. O. Adeyeye, M. E. Welland, and D. M. Tricker, "Single-domain circular nanomagnets," *Phys. Rev. Lett.*, vol. 83, no. 5, pp. 1042–1045, Aug 1999.

[83] M. Klaui, J. Rothman, L. Lopez-Diaz, C. A. F. Vaz, J. A. C. Bland, and Z. Cui, "Vortex circulation control in mesoscopic ring magnets," *Applied Physics Letters*, vol. 78, no. 21, pp. 3268–3270, 2001. [Online]. Available: http://link.aip.org/link/?APL/78/3268/1

[84] E. Saitoh, M. Kawabata, K. Harii, H. Miyajima, and T. Yamaoka, "Manipulation of vortex circulation in decentered ferromagnetic nanorings," *Journal of Applied Physics*, vol. 95, no. 4, pp. 1986–1988, 2004. [Online]. Available: http://link.aip.org/link/?JAP/95/1986/1

[85] M. Natali, I. L. Prejbeanu, A. Lebib, L. D. Buda, K. Ounadjela, and Y. Chen, "Correlated magnetic vortex chains in mesoscopic cobalt dot arrays," *Phys. Rev. Lett.*, vol. 88, no. 15, p. 157203, Apr 2002.

[86] K. Y. Guslienko, V. Novosad, Y. Otani, H. Shima, and K. Fukamichi, "Magnetization reversal due to vortex nucleation, displacement, and annihilation in submicron ferromagnetic dot arrays," *Phys. Rev. B*, vol. 65, no. 2, p. 024414, Dec 2001.

[87] V. Novosad, M. Grimsditch, J. Darrouzet, J. Pearson, S. D. Bader, V. Metlushko, K. Guslienko, Y. Otani, H. Shima, and K. Fukamichi, "Shape effect on magnetization reversal in chains of interacting ferromagnetic elements," *Applied Physics Letters*, vol. 82, no. 21, pp. 3716–3718, 2003. [Online]. Available: http://link.aip.org/link/?APL/82/3716/1

[88] R. P. Cowburn and M. E. Welland, "Room temperature magnetic quantum cellular automata," *Science*, vol. 287, pp. 1466–1468, feb 2000.

[89] M. R. Scheinfein, "Llg micromagnetic simulator."

[90] M. Donahue and D. Porter, "Object oriented micromagnetic framework (oommf)."

[91] T. Shinjo, T. Okuno, R. Hassdorf, K. Shigeto, and T. Ono, "Magnetic Vortex Core Observation in Circular Dots of Permalloy," *Science*, vol. 289, no. 5481, pp. 930–932, 2000. [Online]. Available: http://www.sciencemag.org/cgi/content/abstract/289/5481/930

[92] R. P. Cowburn, A. O. Adeyeye, and M. E. Welland, "Controlling magnetic ordering in coupled nanomagnet arrays," *New Journal of Physics*, vol. 1, pp. 16–+, nov 1999.

ABOUT THE AUTHOR

Anita Kumari received the B.E. degree in electronics and communication engineering from S.L.I.E.T, India, in 2003. She received her MTech. degree in microelectronics from Panjab University, Chd, India, in 2005, and currently pursuing the Ph.D. degree in electrical engineering at University Of South Florida, Tampa, U.S.A. Her research interests include design and modeling of advance nanoscale devices.